



<b>Publication Year</b>	2015
<b>Acceptance in OA@INAF</b>	2020-03-18T15:22:17Z
<b>Title</b>	Chandra Deep Observation of XDCP J0044.0-2033, a Massive Galaxy Cluster at $z > 1.5$
<b>Authors</b>	TOZZI, Paolo; Santos, J. S.; Jee, M. J.; Fassbender, R.; Rosati, P.; et al.
<b>DOI</b>	10.1088/0004-637X/799/1/93
<b>Handle</b>	<a href="http://hdl.handle.net/20.500.12386/23356">http://hdl.handle.net/20.500.12386/23356</a>
<b>Journal</b>	THE ASTROPHYSICAL JOURNAL
<b>Number</b>	799

CHANDRA DEEP OBSERVATION OF XDCP J0044.0-2033, A MASSIVE GALAXY CLUSTER AT  $z > 1.5$ P. TOZZI<sup>1</sup>, J. S. SANTOS<sup>1</sup>, M. J. JEE<sup>2</sup>, R. FASSBENDER<sup>3</sup>, P. ROSATI<sup>1,4</sup>, A. NASTASI<sup>5</sup>, W. FORMAN<sup>6</sup>, B. SARTORIS<sup>7</sup>, S. BORGANI<sup>7,8</sup>, H. BOEHRINGER<sup>9</sup>, B. ALTIERI<sup>10</sup>, G. W. PRATT<sup>11</sup>, M. NONINO<sup>8</sup>, AND C. JONES<sup>6</sup><sup>1</sup> INAF-Osservatorio Astrofisico di Arcetri, Largo E. Fermi 5, I-50125 Firenze, Italy<sup>2</sup> Department of Physics, University of California, Davis One Shields Avenue, Davis, CA 95616-8677, USA<sup>3</sup> INAF-Osservatorio Astronomico di Roma (OAR), via Frascati 33, I-00040 Monte Porzio Catone, Italy<sup>4</sup> Università degli Studi di Ferrara, Via Savonarola, 9 I-44121 Ferrara, Italy<sup>5</sup> Institut d'Astrophysique Spatiale, CNRS, Bat. 121, Université Paris-Sud, F-91405 Orsay, France<sup>6</sup> Harvard-Smithsonian Center for Astrophysics 60 Garden Street, Cambridge, MA 02138, USA<sup>7</sup> Università degli Studi di Trieste, Dipartimento di Fisica, Via A. Valerio, 2 I-34127 Trieste, Italy<sup>8</sup> INAF-Osservatorio Astronomico di Trieste, via G. B. Tiepolo 11, I-34143 Trieste, Italy<sup>9</sup> Max-Planck-Institut für extraterrestrische Physik Giessenbachstr. 1, D-85748 Garching, Germany<sup>10</sup> European Space Astronomy Centre (ESAC), European Space Agency, Apartado de Correos 78, E-28691 Villanueva de la Canada, Madrid, Spain<sup>11</sup> CEA Saclay, Service d'Astrophysique, L'Orme des Merisiers, Bat. 709, F-91191 Gif-sur-Yvette Cedex, France

Received 2014 April 30; accepted 2014 November 14; published 2015 January 19

## ABSTRACT

We report the analysis of the *Chandra* observation of XDCP J0044.0-2033, a massive, distant ( $z = 1.579$ ) galaxy cluster discovered in the XDCP survey. The total exposure time of 380 ks with *Chandra* ACIS-S provides the deepest X-ray observation currently achieved on a massive, high-redshift cluster. Extended emission from the intra cluster medium (ICM) is detected at a very high significance level ( $S/N \sim 20$ ) on a circular region with a  $44''$  radius, corresponding to  $R_{\text{ext}} = 375$  kpc at the cluster redshift. We perform an X-ray spectral fit of the ICM emission modeling the spectrum with a single-temperature thermal *mekal* model. Our analysis provides a global temperature  $kT = 6.7^{+1.3}_{-0.9}$  keV, and a iron abundance  $Z_{\text{Fe}} = 0.41^{+0.29}_{-0.26} Z_{\text{Fe}\odot}$  (error bars correspond to  $1\sigma$ ). We fit the background-subtracted surface brightness profile with a single  $\beta$ -model out to  $44''$ , finding a rather flat profile with no hints of a cool core. We derive the deprojected electron density profile and compute the ICM mass within the extraction radius  $R_{\text{ext}} = 375$  kpc to be  $M_{\text{ICM}}(r < R_{\text{ext}}) = (1.48 \pm 0.20) \times 10^{13} M_{\odot}$ . Under the assumption of hydrostatic equilibrium and assuming isothermality within  $R_{\text{ext}}$ , the total mass is  $M_{2500} = 1.23^{+0.46}_{-0.27} \times 10^{14} M_{\odot}$  for  $R_{2500} = 240^{+30}_{-20}$  kpc. Extrapolating the profile at radii larger than the extraction radius  $R_{\text{ext}}$  we find  $M_{500} = 3.2^{+0.9}_{-0.6} \times 10^{14} M_{\odot}$  for  $R_{500} = 562^{+50}_{-37}$  kpc. This analysis establishes the existence of virialized, massive galaxy clusters at redshift  $z \sim 1.6$ , paving the way to the investigation of the progenitors of the most massive clusters today. Given its mass and the XDCP survey volume, XDCP J0044.0-2033 does not create significant tension with the WMAP-7  $\Lambda$ CDM cosmology.

**Key words:** galaxies: clusters: intracluster medium – galaxies: individual (XDCP J0044.0-2033) – large-scale structure of universe – X-rays: galaxies: clusters

## 1. INTRODUCTION

The search and characterization of distant ( $z > 1$ ) clusters of galaxies has been a major field of research in extragalactic astronomy in the last 10 years. A systematic investigation of galaxy clusters at high redshift can provide at the same time strong constraints on cosmological parameters, on the physics of the intra cluster medium (ICM) and of the interaction of the ICM with cluster galaxies, and on the evolution of the cluster galaxy population. Over the last five years, the number of known clusters at redshift  $z > 1$  has dramatically increased from a few to several tens, while their characterization still remains very challenging. In addition, it is difficult to assemble a sample of high- $z$  clusters with a well-defined selection function, given the wide range of detection techniques used to find the clusters.

At present, there is an increasing effort to build homogeneous and well-characterized samples of high- $z$  clusters based on several complementary approaches. X-ray, infrared (IR), and Sunyaev–Zeldovich (SZ) surveys are the main tools used to build cluster samples. X-ray surveys play a key role in this context. Thanks to the X-ray thermal emission from the ICM, which is the largest baryonic component of galaxy clusters, it is possible to identify galaxy clusters as X-ray extended sources up to

$z > 1$ . This was shown already with the *ROSAT* satellite in the *ROSAT* Deep Cluster Survey (Rosati et al. 2002), where several massive clusters were found up to  $z \sim 1.3$  (Stanford et al. 2001, 2002; Rosati et al. 2004). More recently, the *XMM-Newton* Distant Cluster Project (XDCP; Fassbender et al. 2011a) exploited the capability of *XMM* in identifying high- $z$  cluster candidates, thanks to its large throughput and field of view (FOV). The XDCP has proven to be particularly efficient with 47<sup>12</sup> clusters spectroscopically confirmed to be at  $0.8 < z < 1.6$  (Mullis et al. 2005; Santos et al. 2009; Nastasi et al. 2011, 2014; Fassbender et al. 2011a; Pierini et al. 2012), nearly five times the RDCS sample at  $z > 0.8$ . Other serendipitous surveys based on the archival data of *Chandra*, *XMM-Newton*, and *Swift*-X-ray Telescope archives are ongoing (see Barkhouse et al. 2006; Fassbender et al. 2011a; Clerc et al. 2012; Tozzi et al. 2014), together with fewer dedicated, contiguous survey (Finoguenov et al. 2007; Pierre et al. 2007). For a recent (updated to 2012) summary of the current X-ray cluster surveys, see Tundo et al. (2012).

<sup>12</sup> Among the 47 XDCP clusters at  $z > 0.8$ , 26 are published in the quoted papers, while the remaining 21 spectroscopically confirmed clusters are still unpublished.

IR and SZ surveys are contributing significantly to high-redshift cluster detections (Demarco et al. 2010; Foley et al. 2011; Brodwin et al. 2011, 2012; Stanford et al. 2012; Rettura et al. 2014) and will contribute important samples in the future, particularly due to the lack of a timely, wide-angle, and sensitive X-ray survey. Nevertheless, the X-ray band currently provides the best diagnostics of the dynamical state of the clusters and of the thermo- and chemo-dynamical properties of the ICM and a robust measurement of cluster masses. This can be achieved through the spectral analysis of the ICM emission which provides the mass of the gas and its temperature. Both quantities can be combined to obtain the integrated pseudo-pressure parameter  $Y_X \equiv T_X \times M_{\text{ICM}}$ , considered a robust mass proxy within  $R_{500}$ , as shown by numerical simulations (Kravtsov et al. 2006). Moreover, if the data are sufficiently deep for a spatially resolved analysis, the hydrostatic equilibrium equation can be directly applied to derive a full mass profile. SZ observations are also a direct probe of the ICM; however, the capability of SZ data to characterize the thermodynamics of the ICM is still below that of X-ray data. As of today, the calibration of the SZ mass proxy still relies on a cross-calibration with X-ray data and weak-lensing measurements (Planck Collaboration et al. 2011, 2013; Andersson et al. 2011; von der Linden et al. 2014; Donahue et al. 2014) or dynamical mass estimates (Sifón et al. 2013). Finally, the information that can be derived from optical and IR observations of distant clusters depends critically on how many galaxies are sampled. They give sparse information on the dynamical status and virial mass estimates are strongly dependent on the number of galaxies that are observed.

Up to now, the community has been more interested in pushing the limit toward the most distant clusters, rather than in assembling a well-characterized high- $z$  sample. If we focus on the most distant cluster candidates, we find that only nine clusters have been spectroscopically confirmed at  $z \geq 1.5$  to date and only some of them have estimated masses in excess of  $10^{14} M_{\odot}$  (Brodwin et al. 2011, 2012; Fassbender et al. 2011b; Nastasi et al. 2011; Santos et al. 2011; Zeimann et al. 2012; Stanford et al. 2012). We note that most of these high-redshift clusters have been identified in IR surveys or by combining near infrared and X-ray data.<sup>13</sup> In the last three years a moderate investment of *Chandra* time has been dedicated to the X-ray follow-up observation of some of these clusters at  $z > 1.5$ . However, no prominent, X-ray diffuse emission has been detected, so that no constraints on the cluster dynamical state could be derived (Papovich et al. 2010; Gobat et al. 2011; Pierre et al. 2012). The lack of extended X-ray emission in these systems suggests low X-ray luminosities and points toward a re-classification of these objects as protoclusters. Instead, X-ray emission has been detected in IR-selected clusters at  $z > 1$  but, again, their low X-ray flux did not allow for a detailed analysis (Stanford et al. 2006; Andreon et al. 2009; Brodwin et al. 2011). Only recently, a serendipitously discovered cluster in a deep, ACIS-S *Chandra* observation, allowed us to measure the X-ray redshift and the temperature of a  $z \sim 1.5$  cluster (Tozzi et al. 2013).

In this scenario, deep *Chandra* observations of bona fide X-ray-selected clusters are the only available means to investigate cluster physics at very high- $z$  (see Rosati et al. 2002; Tozzi 2013). These observations are time-expensive but also

extremely valuable, since they allow us to peer into an epoch, at a lookback time larger than 9 Gyr ( $z > 1.5$ ), which recent observations indicate is key for the assembly of cluster mass and the inversion of the star-formation–density relation in cluster galaxies. Given the large amount of time needed to observe clusters at such a high redshift, a crucial requirement is to have an X-ray-selected target, whose diffuse X-ray emission has been unambiguously assessed. As matter of fact, any deep *Chandra* observation of a distant, bona fide cluster is providing a secure scientific return which will be unrivaled until the next generation of high-angular resolution X-ray satellites.<sup>14</sup> This strategy has been shown to be highly successful for XMMU J2235.3-2557 observed for 200 ks with *Chandra* ACIS-S (Rosati et al. 2009), and whose accurate mass estimate has triggered a large number of theoretical speculations on its cosmological implications (e.g., Sartoris et al. 2010; Mortonson et al. 2011; Harrison & Coles 2012).

In this paper we present the deep, 380 ks *Chandra* observation of XDCP J0044.0-2033 (hereafter XDCP0044) at  $z = 1.58$  (Santos et al. 2011), the X-ray-selected distant cluster with the largest estimated mass at  $z > 1.5$ . XDCP0044 was discovered serendipitously in the *XMM-Newton* data in the XDCP. The *XMM* discovery data, however, allows only a robust measure of the X-ray luminosity of the most distant clusters (Fassbender et al. 2011a) and only fairly uncertain masses, simply based on scaling relations, can be derived. The *Chandra* data presented in this work constitutes the deepest X-ray observation to date on a cluster at  $z > 1.0$ .

The paper is organized as follows. In Section 2 we describe the discovery data and give a brief summary of the available multi-wavelength data set. Then we present our X-ray data reduction procedure and spectral analysis, which provides us with global temperature and iron abundance. We also investigate the surface brightness properties of the ICM. In Section 3 we derive the ICM mass and the total cluster mass for a given density contrast with respect to the critical value. In Section 4 we discuss the systematics on the mass measurements, the cosmological implications, the possible presence of substructures in the ICM, and briefly discuss the future of high- $z$  cluster studies in the light of planned X-ray missions. Finally, our conclusions are summarized in Section 5. Throughout the paper, we adopt the seven-year *Wilkinson Microwave Anisotropy Probe* (WMAP) cosmology ( $\Omega_{\Lambda} = 0.73$ ,  $\Omega_m = 0.27$ , and  $H_0 = 70.4 \text{ km s}^{-1} \text{ Mpc}^{-1}$ ) (Komatsu et al. 2011). In this cosmology,  $1''$  on the sky corresponds to 8.554 kpc at  $z = 1.58$ . Quoted errors always correspond to a  $1\sigma$  confidence level.

## 2. CLUSTER IDENTIFICATION AND X-RAY DATA ANALYSIS

### 2.1. Discovery Data and Multi-wavelength Data Set

XDCP0044 was serendipitously detected in the archive of the X-ray observatory *XMM-Newton* by the XDCP as an extended source at  $5\sigma$  c.l. at an off-axis angle of  $10'8$  and J2000 coordinates R.A. =  $00^{\text{h}}44^{\text{m}}05^{\text{s}}.2$ , decl. =  $-20^{\circ}33'59''.7$ , with an effective exposure time of 8.5 ksec. The unabsorbed

<sup>13</sup> The most distant confirmed SZ-selected clusters to date are reported at  $z \sim 1.32$  (Stalder et al. 2013) and  $z = 1.478$  (Bayliss et al. 2014).

<sup>14</sup> At present, the only future mission which foresees an improvement with respect to the *Chandra* optics is SMART-X, see <http://smart-x.cfa.harvard.edu/doc/2011-10-smartx-rfi-response.pdf>. The planned mission Athena (Barcons et al. 2012; Nandra et al. 2013) will have a much larger effective area on a significantly larger field of view, however, the current requirements on the angular resolution correspond at best to  $5''$  HEW (see <http://www.the-athena-x-ray-observatory.eu/>).



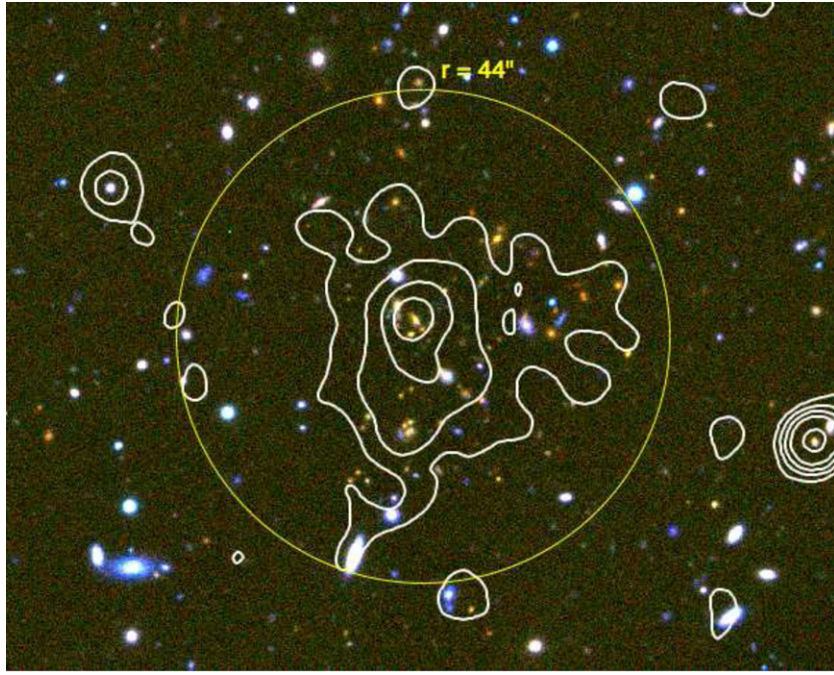


**Figure 1.** Optical *IJKs* color image of XDCP0044 with *Chandra* smoothed soft-band contours overlaid. Contours correspond to levels of 0.11, 0.3, 0.6 and 1.0 counts per pixel, to be compared with a background level of  $3.5 \times 10^{-2}$  counts per pixel in the original image (1 pixel =  $0''.492$ ). The image is obtained from Subaru/Suprime-Cam (*V* and *i* bands) and Hawk-I at VLT (*J* and *Ks* band) and has a size of  $2'.5 \times 2'$ . The solid circle has a radius of  $44''$  (corresponding to 375 kpc at  $z = 1.58$ ), and shows the region used for the X-ray spectral analysis.

flux is measured from *XMM-Newton* data to be  $S_{0.5-2.0} = (1.6 \pm 0.3) \times 10^{-14}$  erg s $^{-1}$  cm $^{-2}$  based on the growth curve analysis, within a radius of  $35''$ , corresponding to 296 kpc at  $z = 1.58$ .

We detected a galaxy overdensity associated with the diffuse X-ray emission using medium-deep imaging in *I* and *H* bands from EFOSS and SOFI, respectively, at ESO/NTT. The color image with X-ray contours overlaid is shown in Figure 1. Subsequent optical spectroscopy from Very Large Telescope (VLT)/FORS2 later confirmed the cluster redshift by identifying three cluster members (Santos et al. 2011). Recently, new VLT/FORS2 spectroscopy secured four other cluster members, bringing the total to seven already published in the literature (Fassbender et al. 2014). Most recent progress in optical spectroscopy added at least five new secure cluster members, bringing the total number of confirmed members to twelve (A. Nastasi et al. in preparation). Among the twelve confirmed members, six are within  $20''$  from the X-ray center, and therefore are embedded in the ICM extended emission.

Since the discovery of XDCP0044, we have embarked on a demanding observational campaign, given the uniqueness of this system. Currently, our multi- $\lambda$  data set includes deep *J/Ks* imaging from VLT/Hawk-I presented in Fassbender et al. (2014), additional VLT/FORS2 data providing the twelve confirmed cluster members previously mentioned, recent VLT/KMOS infrared IFU spectroscopy which will augment our sample of cluster members, as well as mid-to-far infrared imaging from *Spitzer* (M. Verdugo et al., in preparation) and *Herschel* (Santos et al. 2015). In addition to our dedicated programs, we also have access to deep, wide-field imaging in *I* and *V* bands from Subaru/Suprime-Cam. The analysis of this data, to be published in forthcoming papers, will provide a detailed characterization of the galaxy population of this massive, high- $z$  cluster, giving important clues on galaxy evolutionary

processes, such as the amount and distribution of star formation in the cluster members.

## 2.2. X-Ray Data Reduction

XDCP0044 was observed with a *Chandra* Large Program observation of 380 ks with ACIS-S granted in Cycle 14 (PI P. Tozzi). The observations were completed in the period 2013 October–December. The nominal total exposure time excluding the dead-time correction (corresponding to the LIVETIME keyword in the header of *Chandra* fits files) amounts to 371.6 ks.

We performed a standard data reduction starting from the level = 1 event files, using the CIAO 4.6 software package, with the most recent version of the Calibration Database (CALDB 4.6.3). Since our observation is taken in the VFaint mode we ran the task `acis_process_events` to flag background events that are most likely associated with cosmic rays and distinguish them from real X-ray events. With this procedure, the ACIS particle background can be significantly reduced compared to the standard grade selection. The data is filtered to include only the standard event grades 0, 2, 3, 4, and 6. We checked visually for hot columns left after the standard reduction. For exposures taken in VFaint mode, there are practically no hot columns or flickering pixels left after filtering out bad events. We finally filter time intervals with high background by performing a  $3\sigma$  clipping of the background level using the script `analyze_1tcrv`. The final useful exposure time amounts to 366.8 ks. The removed time intervals therefore amount to 4.8 ks, about 1.3% of the nominal exposure time. We remark that our spectral analysis is not affected by any possible undetected flare, since we are able to compute the background in the same observation from a large, source-free region around the cluster, thus taking into account any possible spectral distortion of the background itself induced by unnoticed flares. Eventually, we

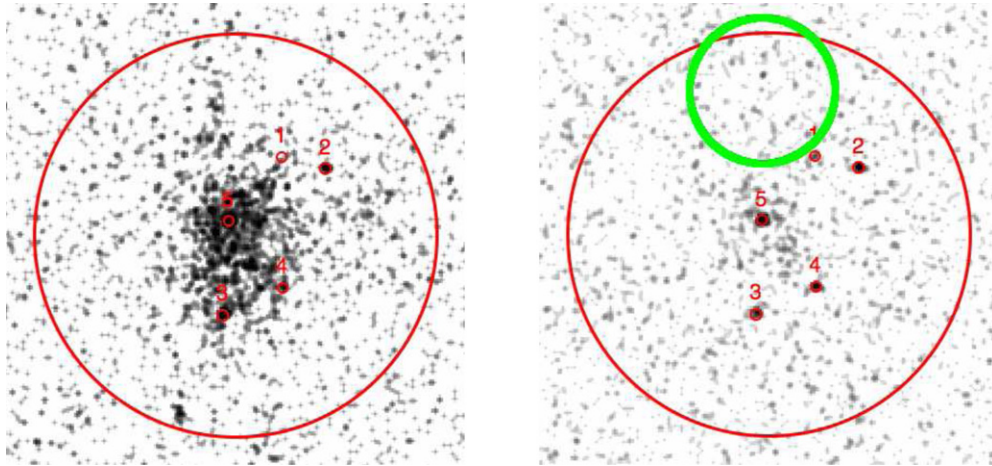


**Figure 2.** *Chandra* image of XDCP0044 in the soft 0.5–2 keV band (left panel) and in the hard 2–7 keV band (right panel). The image has not been rebinned (1 pixel corresponds to  $0''.492$ ). The large red circle shows the extraction region used for the spectral analysis, corresponding to  $R_{\text{ext}} = 44'' = 375$  kpc at  $z = 1.58$ . The five small circles show the unresolved sources identified in the soft- or in the hard-band images. The green circle in the hard-band image shows the uncertainty in the position of the radio source NVSS 004405–203326. Images are  $1.7 \times 1.7$  arcmin across.

**Table 1**  
Aperture Photometry of the Five Unresolved Sources Identified within the X-Ray Extended Emission of XDCP0044

Source No.	Soft Counts (0.5–2 keV)	Hard Counts (2–7 keV)	Soft Flux (0.5–2 keV)	Hard Flux (2–10 keV)	Redshift
1	$1.8 \pm 2.0$	$7.8 \pm 3.0$	...	$(5.6 \pm 2.2) \times 10^{-16}$	...
2	$15.2 \pm 4.1$	$29.0 \pm 5.5$	$(2.0 \pm 0.5) \times 10^{-16}$	$(2.1 \pm 0.4) \times 10^{-15}$	...
3	$40.0 \pm 7.0$	$20.0 \pm 5.0$	$(5.4 \pm 0.9) \times 10^{-16}$	$(1.4 \pm 0.4) \times 10^{-15}$	1.5703
4	$8.4 \pm 3.7$	$25.8 \pm 5.3$	$(1.1 \pm 0.5) \times 10^{-16}$	$(1.9 \pm 0.4) \times 10^{-15}$	0.5922
5	$122.0 \pm 12.0$	$117.0 \pm 11.0$	$(1.6 \pm 0.15) \times 10^{-15}$	$(8.4 \pm 0.8) \times 10^{-15}$	1.5785

**Notes.** The photometry corresponds to the net number of counts detected within an aperture radius of  $2''.5$  in the soft- (0.5–2 keV) and hard-band (2–7 keV) images after background subtraction. Energy fluxes are obtained in the soft and hard (2–10 keV) bands assuming a power law spectra with photon index  $\Gamma = 1.4$  and taking into account Galactic absorption. Sources 3 and 5 are confirmed cluster members, while source 4 is a foreground AGN.

will explore the dependence of our results on the background choice, including also a synthetic background.

### 2.3. Point Source Removal and Aperture Photometry

In Figure 2 we show a close-up of the XDCP0044 X-ray image in the soft (left panel) and hard (right panel) bands. By running the *ciao* detection algorithm *wavdetect* we identify five unresolved sources overlapping with the ICM emission. We carefully check by eye that the detection algorithm kept the unresolved and the surrounding extended emission well separated, to be able to remove only the unresolved source contribution and eventually extract the ICM emission free from active galactic nucleus (AGN) contamination. We measure the aperture photometry for the five unresolved sources within a radius of  $2''.5$ , which is expected to include about 90% of the flux, exploiting the exquisite angular resolution of *Chandra* close to the aimpoint. The background is estimated locally in an annulus around each source (outer radius  $10''$ , inner radius  $5''$ ) in order to accurately take into account the surrounding extended emission. The approximate soft- and hard-band fluxes are computed after correcting for vignetting and assuming the typical conversion factors in the soft and hard band corresponding to a power law emission with photon index  $\Gamma = 1.4$ . Considering the effective area of each single exposure at the position of the cluster, and assuming a Galactic absorption column density of  $N_{\text{H}} = 1.91 \times 10^{20} \text{ cm}^{-2}$  (see next section), we obtain  $C_{\text{soft}} = 4.93 \times 10^{-12} \text{ cgs/}$

counts/s and  $C_{\text{hard}} = 2.64 \times 10^{-11} \text{ cgs/counts/s}$ . We find that the total soft-band flux contributed by point sources is about 12% of the diffuse emission, in line with what is found in non X-ray-selected clusters (see, e.g., Bignamini et al. 2008). Incidentally, this confirms that the presence of X-ray-emitting AGN within the extended emission of distant clusters does not hamper one from identifying them even with moderate angular resolution. The results are shown in Table 1. Note that while the net detected counts in the hard band refer to the 2–7 keV energy range, we compute the energy fluxes in the 2–10 keV band, for a better comparison with the literature, despite our unresolved sources showing very little signal above 7 keV. At least two of them (3 and 5) are cluster members, and one (4) is a foreground AGN. The two unidentified X-ray sources are likely to be foreground AGN due to their hard X-ray emission. A further X-ray source is just on the edge of the extraction regions, and it is identified with a foreground galaxy. There are other unresolved X-ray sources within the virial radius of the cluster, which potentially can be cluster members. A more detailed discussion of the cluster galaxy population, including their X-ray properties, will be presented in forthcoming papers.

The nature of the X-ray extended emission after the removal of the unresolved source contribution can be safely assumed to be entirely due to the thermal bremsstrahlung from the ICM. We can exclude a significant contribution from inverse-Compton emission associated with a population of relativistic

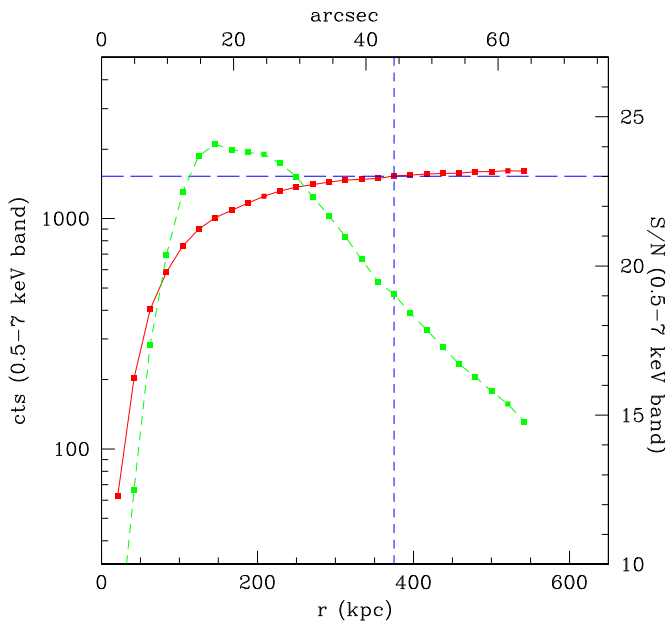


**Figure 3.** Solid red line shows the aperture photometry in the total (0.5–7 keV) band for XDCP0044 as a function of the physical projected radius. The dashed vertical line is the extraction radius used for spectral analysis, corresponding to  $R_{\text{ext}} = 375$  kpc. The green dashed line is the measured S/N within a given radius. The horizontal line is the photometry measured within  $R_{\text{ext}}$  corresponding to  $1500 \pm 80$  net counts in the 0.5–7 keV band.

electrons, since such a component would result in radio emission visible with NVSS data. The NVSS radio image shows no radio emission in the direct vicinity of the X-ray center. However, the NVSS catalog reports a weak radio source, NVSS 004405-203326, at a distance of  $33''$  from the cluster center, with an estimated flux of  $3.2 \pm 0.6$  mJy at 1.4 GHz and an uncertainty in the position of about  $15''$  (Condon et al. 1998). The position of the radio source is shown as a green circle in Figure 2, right panel, and it is clearly unrelated to the X-ray emission.

We perform simple aperture photometry of the extended emission after removing the detected point sources. First, we compute the centroid of the X-ray emission, by searching the position where the aperture photometry within a fixed radius of 100 kpc returns the highest signal-to-noise (S/N) in the 0.5–7 keV band. We find that the center of the X-ray emission is in  $\text{R.A.}_X = 00^{\text{h}}44^{\text{m}}05^{\text{s}}.27$ ,  $\text{decl.}_X = -20^{\circ}33'59''.4$ . We also notice that given the flat and irregular surface brightness distribution, the X-ray centroid can vary by  $\sim 3''$  when the aperture radius ranges between 20 and 200 kpc. Therefore, despite the lack of a well-defined peak in the surface brightness distribution, the X-ray centroid is relatively stable and in excellent agreement with the *XMM* position.

The background is estimated from an annulus centered on the cluster and distant from the cluster emission. The outer radius of the background annulus is  $137''$ , while the inner radius is  $79''$ . Clearly all the identified unresolved sources in the background region are removed before extracting the spectrum. We measure a background of  $3.8 \times 10^{-7}$  counts/s/arcsec<sup>2</sup> in the 0.5–2 keV band and  $6.2 \times 10^{-7}$  counts/s/arcsec<sup>2</sup> in the 2–7 keV band. The total net counts detected in the 0.5–7 keV band as a function of the physical projected radius are shown in Figure 3. We find  $1500 \pm 80$  net counts within 375 kpc. The extended emission lost because of the removal of circular regions of radius  $2\frac{1}{2}$  around unresolved sources has been estimated to be  $\sim 20$  net counts

in the same band, about 1.3%, well below the  $1\sigma$  poissonian uncertainty (about  $\sim 5\%$ ).

We also investigate whether our choice of the background affects the photometry, and, eventually, the spectral analysis. We repeat the photometry with a synthetic background obtained by processing the *Chandra* ACIS blank sky files in the same way we processed our data.<sup>15</sup> We reproject the background events according to each separate ObsID, and normalize the background for each ObsID by choosing source-free regions in the actual data in several different regions of the detector and requiring the same 0.5–7 keV average count rate. We finally obtain a synthetic background image we can use to subtract to the data image. With this procedure we find  $1494 \pm 84$  net counts, consistent well within  $1\sigma$  with the photometry based on the local background.

#### 2.4. Spectral Analysis: Temperature and Iron Abundance

We perform a spectral analysis of the ACIS-S data with *Xspec* v12.8.1 (Arnaud 1996). The adopted spectral model is a single-temperature *mekal* model (Kaastra 1992; Liedahl et al. 1995), using as a reference the solar abundance of Asplund et al. (2005). The local absorption is fixed to the Galactic neutral hydrogen column density measured at the cluster position and equal to  $N_{\text{H}} = 1.91 \times 10^{20} \text{ cm}^{-2}$  taken from the LAB Survey of Galactic H I (Kalberla et al. 2005). The fits are performed over the energy range 0.5–7.0 keV. We used Cash statistics applied to the source plus background, which is preferable for low S/N spectra (Nousek & Shue 1989).

We extract the cluster emission from a circle of radius  $R_{\text{ext}} = 44''$ , corresponding to 375 kpc at  $z = 1.58$ . This radius is chosen in order to encompass the maximum signal ( $\sim 1500$  net counts in the 0.5–7 keV band; see Figure 3). Beyond the radius  $R_{\text{ext}}$ , the residual signal is consistent with zero within the statistical  $1\sigma$  error on photometry. The spectrum of the total emission within the extraction radius, after the removal of the five unresolved sources discussed in Section 2.3, is fitted with the single-temperature *mekal* model. First, we leave the redshift parameter free to vary, but we are not able to obtain a reliable measurement of the X-ray redshift  $z_X$ . For *Chandra* observations, it was estimated that about 1000 net counts are needed to measure  $z_X$  at a  $3\sigma$  confidence level, and even more are needed in the case of hot clusters, as shown in Yu et al. (2011) for medium exposures ( $\sim 100$  ks). In the case of XDCP0044, the large exposure time also implies a relatively larger background and lower S/N with respect to the typical case explored in Yu et al. (2011), and this prevents us from retrieving the correct redshift directly from the X-ray spectral analysis, even with  $\sim 1500$  net counts. Then, we set the redshift to  $z = 1.58$  and find that the best-fit global temperature is  $kT = 6.7^{+1.3}_{-0.9}$  keV. The measured iron abundance, in units of Asplund et al. (2005), is  $Z_{\text{Fe}} = 0.41^{+0.29}_{-0.26} Z_{\text{Fe}\odot}$ . The cluster unabsorbed soft-band flux within a circular region of  $44''$  radius is  $S_{0.5-2.0\text{keV}} = (1.66 \pm 0.09) \times 10^{-14} \text{ erg s}^{-1} \text{ cm}^{-2}$  (in excellent agreement with the soft flux estimated from the *XMM-Newton* discovery data), and the hard flux  $S_{2-10\text{keV}} = (1.41 \pm 0.07) \times 10^{-14}$ . At a redshift of  $z = 1.58$  this corresponds to a rest frame soft-band luminosity of  $L_S = (1.89 \pm 0.11) 10^{44} \text{ erg s}^{-1}$ . The X-ray bolometric luminosity is  $L_{\text{bol}} = (6.8 \pm 0.4) 10^{44} \text{ erg s}^{-1}$ . In Figure 4 we show the spectrum of XDCP0044 within a radius of 375 kpc along with the best-fit model.

<sup>15</sup> <http://cxc.harvard.edu/ciao/threads/acisbackground/>



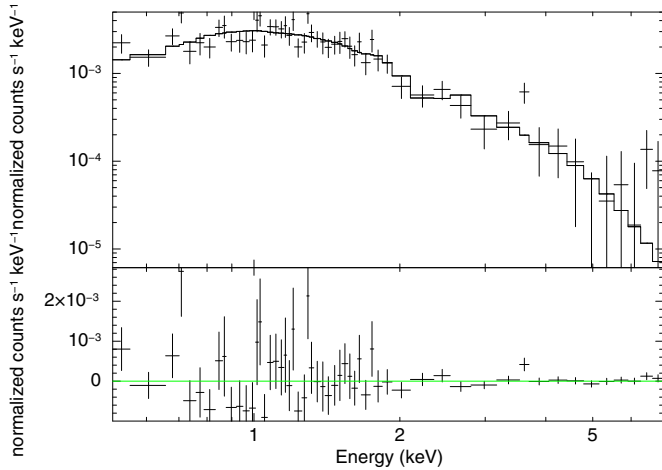


**Figure 4.** Folded *Chandra* ACIS-S spectrum of XDCP0044 within 44'' (375 kpc) with its best-fit *mekal* model (solid line). The presence of the iron  $K_{\alpha}$  lines complex, expected at 2.6 keV in the observed reference frame, has a statistical significance below  $2\sigma$ . The lower panel shows the residuals. The spectrum has been binned with a minimum of 25 counts per bin only for plotting purpose.

We also perform the spectral analysis in the region with the maximum S/N, corresponding to a radius of 17'' (145 kpc; see Figure 3). This region includes about two-thirds of the signal we found in the  $R_{\text{ext}} = 44''$  region. We obtain  $kT = 5.9^{+0.8}_{-0.5}$  and  $Z_{\text{Fe}} = 0.28^{+0.20}_{-0.18} Z_{\text{Fe}\odot}$ . In this case, if the redshift is left free, we are able to recover a best-fit redshift of  $z_X = 1.59^{+0.08}_{-0.06}$ . Despite this value being in perfect agreement with the optical redshift, the significance level of the X-ray redshift is still below  $2\sigma$ .

We highlight that, in both cases, the measured iron abundance is consistent with zero within  $2\sigma$ . This marginal detection does not allow us to draw any conclusion on the possible evolution of the iron abundance of the ICM in XDCP0044 with respect to local clusters. However, this finding is consistent with the mild, negative evolution of the iron abundance of a factor 1.5–2 between  $z = 0$  and  $z \sim 1$  found in previous works (Balestra et al. 2007; Maughan et al. 2008; Anderson et al. 2009; Baldi et al. 2012). We conclude that, despite our expectations, we are not able to use XDCP0044 to put significant constraints on the iron enrichment timescale in the ICM. This study is currently limited to the brightest clusters at  $z \sim 1$  (see De Grandi et al. 2014). A systematic investigation of the iron abundance evolution in very high- $z$  clusters requires higher sensitivity, and it will be an important science case for future X-ray facilities such as Athena (Barcons et al. 2012; Nandra et al. 2013) and SMART-X.<sup>16</sup>

We also attempt a spatially resolved spectral analysis dividing the ICM emission in five annular bins with about 300 net counts each. We tentatively find a hint of a decreasing temperature beyond 100 kpc, as shown in Figure 5, which also explains the 1 $\sigma$  difference between the two extraction regions at 44'' and 17''. We perform a preliminary study to investigate whether this decrease may be associated with a difference in temperature in two different regions of the clusters. To do that, we identify, by visual inspection, two clumps (north and south) as shown in Figure 6 where the extraction regions are drawn manually. The two clumps are identified based on a significant difference in the average surface brightness, which in the north clump is measured to be about 1.8 times higher than in the south clump at more than  $4\sigma$  confidence level. The reliability of the

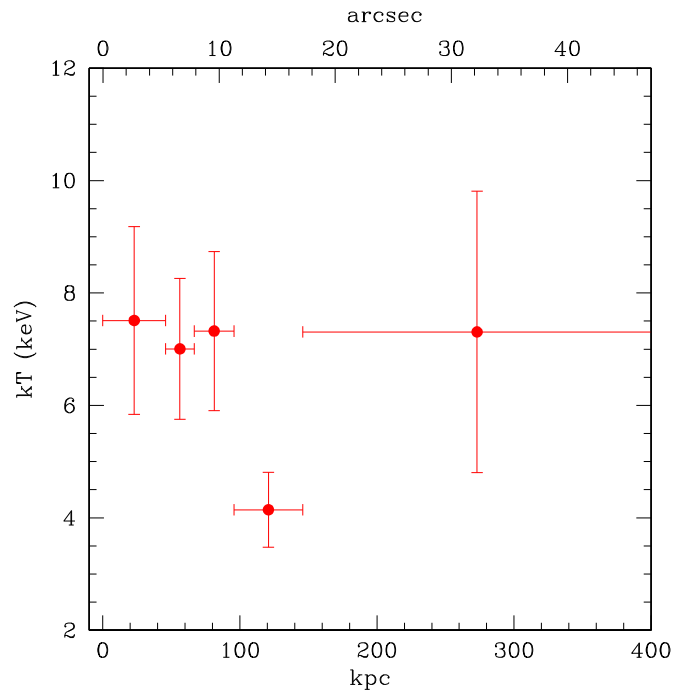


**Figure 5.** Projected temperature profile from the spatially resolved spectral analysis of XDCP0044. Each bin includes about 300 net counts in the 0.5–7 keV band.

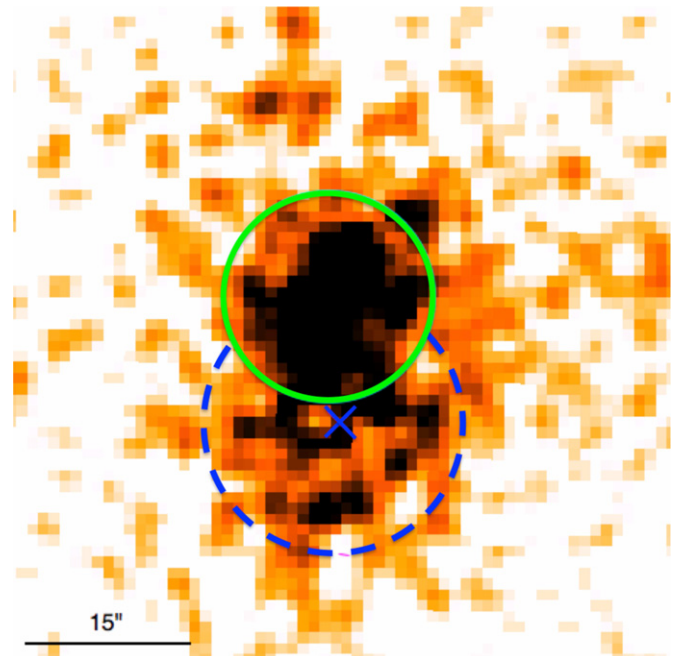


**Figure 6.** North and south clumps of XDCP0044 identified by visual inspection. The extraction region of the north clump is given by the entire circular region (green solid line), while for the south clump is given by a circular region after excluding the overlap with the north region (dashed blue circle).

existence of two physically different regions is also suggested by the observed discontinuity in the surface brightness profile at a distance from the center corresponding to the dividing line of the north and south clumps (see Section 2.5). The north clump is identified by a circular region centered on  $00^{\text{h}}44^{\text{m}}05^{\text{s}}.4$ ,  $-20^{\circ}33'56''.2$  with a radius of 10''. The south clump is identified by a circular region centered on  $00^{\text{h}}44^{\text{m}}05^{\text{s}}.3$ ,

<sup>16</sup> <http://smart-x.cfa.harvard.edu/>

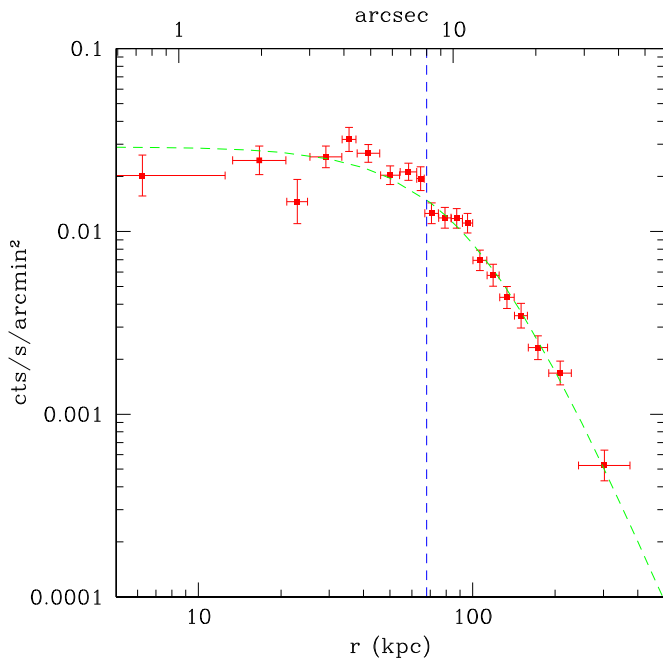


**Figure 7.** Background-subtracted surface brightness profile in the soft (0.5–2 keV) band (points) and best-fit  $\beta$  model (green dashed line) for XDCP0044. Error bars correspond to  $1\sigma$  uncertainty. The vertical dashed line corresponds to the distance of the border of the northern clump from the X-ray centroid.

$-20^{\circ}34'07''.6$  and a radius of  $12''$ , with the exclusion of the part overlapping with the north clump. The distance between the center of the two clumps amounts to  $11''.6$ , corresponding to  $\sim 100$  kpc. The soft-band fluxes in the north and south clumps are  $5.4 \times 10^{-15}$  erg cm $^{-2}$  s $^{-1}$  and  $3.5 \times 10^{-15}$  erg cm $^{-2}$  s $^{-1}$ , respectively. For the north clump we obtain  $kT = 7.1^{+1.3}_{-1.0}$  keV and for the south clump  $kT = 5.5^{+1.2}_{-1.0}$  keV. The difference is comparable to the  $1\sigma$  uncertainty and therefore we are not able to confirm a temperature gradient between the two regions. However, this finding, coupled to the irregular appearance of the surface brightness of XDCP0044, points toward a complex dynamical state of the cluster. Another hint is an extension of diffuse emission for approximately 15 kpc above the north clump (see Figure 6). However, in this case the emission is too faint to attempt a spectral analysis. Finally, a wide western extension is also visible in the contours in Figure 1. Despite these hints for a complex, not spherically symmetric morphology, in the rest of the paper we will assume spherical symmetry to measure the gas and total masses as a function of radius, a choice which is tested in Section 2.5. Further discussion on the presence of substructures in the ICM is postponed to Section 4. For the same reason, we will rely on the spectral analysis of the emission within  $R_{\text{ext}} = 44''$ , which includes the maximum useful signal.

Finally, we investigate whether our spectral analysis is robust against different choices of the background. We repeat the spectral analysis using the synthetic background extracted from the same background region and from the same source region of our data. We remind that the synthetic background is obtained summing the contribution of the synthetic background for each ObsID, where the count rate in the 0.5–7 keV band is normalized to that measured in the data within the same region. Using the synthetic background spectrum extracted from the background region, we find  $kT = 7.8^{+1.5}_{-1.3}$  keV and  $Z_{\text{Fe}} = 0.19^{+0.26}_{-0.19} Z_{\text{Fe}\odot}$ .

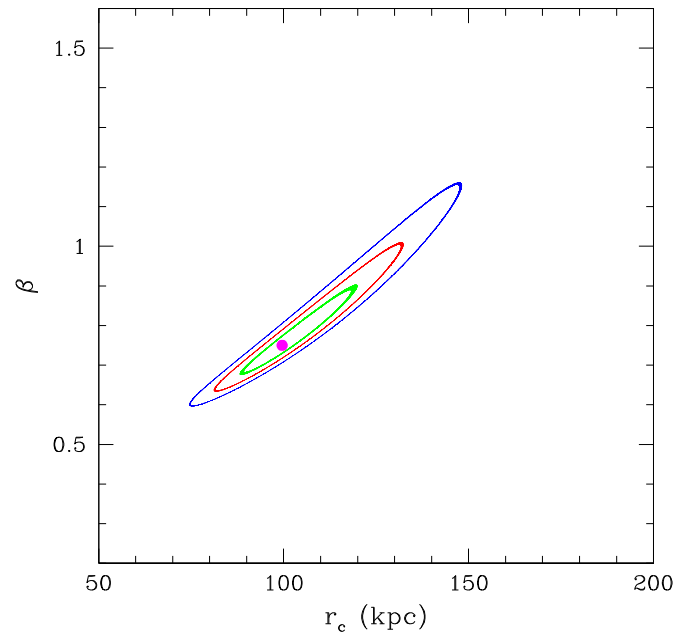


**Figure 8.** Green, red and blue contours show the  $1\sigma$ ,  $2\sigma$ , and  $3\sigma$  confidence levels, respectively, for two relevant parameters  $\beta$  and  $r_c$  of the surface brightness profile.

If, instead, we use the synthetic background extracted from the source region, we find  $kT = 8.2^{+2.0}_{-1.5}$  keV,  $Z_{\text{Fe}} = 0.40^{+0.35}_{-0.33} Z_{\text{Fe}\odot}$ . In general, the use of a synthetic background normalized to the 0.5–7 keV count rate in the data provides slightly harder spectra, and therefore higher temperatures. However, the difference is always consistent within  $1\sigma$  with our analysis based on the local background. In the rest of the paper, we will rely only on the spectral analysis obtained with the local background.

## 2.5. Surface Brightness Profile and Concentration

We compute the azimuthally averaged surface brightness profile from the exposure-corrected ACIS-S image in the soft band out to  $R_{\text{ext}} = 44''$  and centered on R.A. $_X = 00^{\text{h}}44^{\text{m}}05^{\text{s}}.27$ , decl. $_X = -20^{\circ}33'59''.4$ . The profile is well described by a single  $\beta$  model,  $S(r) = S_0(1+(r/r_c)^2)^{-3\beta+0.5} + \text{bkg}$  (Cavaliere & Fusco-Femiano 1976). The azimuthally averaged surface brightness profile and its best-fit model are shown in Figure 7. We note that the surface brightness distribution in the core region is noisy, and this does not depend on the choice of the X-ray center. Incidentally, we remark that the first bin is a circle with a radius of 3 pixels, corresponding to  $1''.5$ , which is the smallest region that can be resolved by *Chandra* at the aimpoint. As we already mentioned, this suggests a lack of a well developed core. The best-fit parameters are  $\beta = 0.75 \pm 0.04$  and core radius  $r_c = 100 \pm 10$  kpc for a reduced  $\chi^2 = 1.37$ . The surface brightness profile is well rendered by the  $\beta$ -model and it allows us to derive accurate gas mass measurements despite the degeneracy between the parameters  $\beta$  and  $r_c$  (see Figure 8). However, the extrapolation of the surface brightness profile at radii larger than  $R_{\text{ext}}$  is uncertain, and further assumptions are needed to estimate the total mass beyond this radius. We also note that the azimuthally averaged surface brightness profile shows some irregularities. However, we detect a discontinuity in the surface brightness profile at a radius of  $\sim 70$  kpc, at a  $2\sigma$  confidence level. We argue that this feature may be associated with the presence of the two clumps discussed in



Section 2.4. In fact, the center of the northern clump is only  $3''$  from the center of the overall X-ray emission, used to compute the azimuthally averaged surface brightness. Since the radius of the northern clump is  $10''$ , the distance where the surface brightness starts to be sampled beyond the northern clump is roughly 70 kpc. Therefore, the jump in the azimuthally averaged surface brightness profile exactly at 70 kpc can be ascribed to the sudden change in surface brightness outside the northern clump. This finding, despite having low statistical significance, provides another hint of a physical difference between the two regions, possibly associated with an ongoing or recent merger, or with a very recent virialization for the bulk of the cluster.

We also attempt a double  $\beta$  model fit, and we find an improvement in the  $\chi^2$  of  $\Delta\chi^2 \sim 2.4$ , while the reduced  $\tilde{\chi}^2 = 1.50$  is higher than in the single  $\beta$  model fit, showing no significant improvements. Furthermore, the measurement of the source profile in sectors is not feasible given the low signal. Therefore, we conclude that the assumption of spherical symmetry and the use of a single  $\beta$  model are fully acceptable for our data, while more complex models would introduce unnecessary degrees of freedom.

From the surface brightness profile we can compute the correction factor to be applied to the measured luminosity within  $R_{\text{ext}}$  to obtain the total luminosity within the virial radius. This factor is 1.11–1.13 for  $R_{\text{vir}} = 800$ –1000 kpc. Applying this factor to the luminosity measured within  $R_{\text{ext}}$  most likely provides an upper limit to the total luminosity, given that surface brightness profiles are generally observed to steepen in the outer regions with respect to the extrapolation of the  $\beta$ -fit model (Ettori & Balestra 2009).

As already mentioned, the surface brightness profile within 100 kpc does not support the presence of a cool core. To quantify the core strength, we compute the value of  $c_{\text{SB}}$ , a concentration parameter defined in Santos et al. (2008) as the ratio of the surface brightness within 40 kpc and 400 kpc:  $c_{\text{SB}} = \text{SB}(<40 \text{ kpc}) / \text{SB}(<400 \text{ kpc})$ . A cluster is expected to host a cool core if  $c_{\text{SB}} > 0.075$ . This simple phenomenological parameter has proven to be a robust cool core estimator, particularly in low S/N data typical of distant clusters. We measured  $c_{\text{SB}} = 0.12 \pm 0.02$ , which is  $2\sigma$  above the minimum  $c_{\text{SB}}$  expected for a cool-core cluster. However, in the case of XDCP0044 we notice that the surface brightness is well sampled only within  $\sim 100$  kpc, much less than the reference radius of 400 kpc, and this may introduce some errors in the measured  $c_{\text{SB}}$  value. If we compare the best-fit profile of the electron density of XDCP0044 with that of the high- $z$  cool-core cluster WARP1415 (Santos et al. 2012), we see a remarkable difference, despite the similar measured  $c_{\text{SB}}$ . Actually, the  $n_e(r)$  profile of XDCP0044 is very similar to that of CXO1415 (Tozzi et al. 2013), a comparable massive cluster at  $z \sim 1.5$ . If we use the temperature and electron density measured within 100 kpc, we find a central entropy of  $94^{+19}_{-14}$  keV cm<sup>2</sup>, corresponding to an average cooling time of  $4.0^{+0.9}_{-0.6}$  Gyr for an iron abundance  $\sim 0.4 Z_{\text{Fe}\odot}$ . Despite these being average values within 100 kpc, the rather flat density profile and the lack of any hint of a temperature drop within 100 kpc suggest that these values are representative of the cluster inner region, and clearly classify XDCP0044 as a non-cool core cluster. Since cool cores are already established at  $z \sim 1$  (Santos et al. 2012), we may begin to identify a population of massive clusters at an epoch before the cool core appearance. Clearly this can be tested only with much larger statistics and high quality data, a goal that

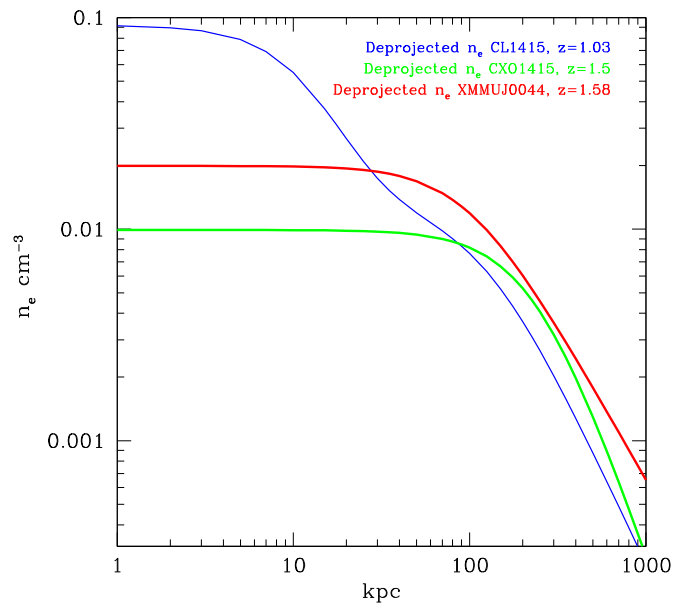


**Figure 9.** Best-fit to the deprojected electron density profile of XDCP0044 (red line) compared with those of CXO1415 (green line; Tozzi et al. 2013) and W1415 (blue line; Santos et al. 2012).

is challenging given the limited discovery space of present-day X-ray observatories.

### 3. GAS MASS AND TOTAL MASS

The baryonic mass can be directly computed once the three-dimensional electron density profile is known. For a simple  $\beta$  model, this is given by  $n_e(r) = n_{e0}[(1 + (r/r_c)^2)^{-3\beta/2}]$ . To measure  $n_{e0}$ , we use the relation between the normalization of the X-ray spectrum and the electron and proton density in the ICM for the meka1 model:

$$\text{Norm} = \frac{10^{14}}{4\pi D_a^2 (1+z)^2} \times \int n_e n_H dV, \quad (1)$$

where  $D_a$  is the angular diameter distance to the source (cm),  $n_e$  and  $n_H$  (cm<sup>-3</sup>) are the electron and hydrogen densities, respectively, and the volume integral is performed over the projected region used for the spectral fit. For XDCP0044, this gives a central electron density of  $n_{e0} = (2.15 \pm 0.13) \times 10^{-2}$  cm<sup>-3</sup>. The physical three-dimensional electron density distribution can be obtained simply by deprojecting the best-fit  $\beta$ -model.

In Figure 9 we show the analytical best fit of the electron density  $n_e(r)$  compared with that found in W1415 and CXO1415. The former is a  $z \sim 1$  strong cool-core cluster with a lower temperature (Santos et al. 2012), showing a density profile strikingly different from that of XDCP0044. On the other hand, the density profile of XDCP0044 is quite similar to that of CXO1415, a comparable,  $z \sim 1.5$  cluster with a lower luminosity and a comparable global temperature  $kT = 5.8^{+1.2}_{-1.0}$  keV (Tozzi et al. 2013). The difference in luminosity (the bolometric luminosity of XDCP0044 is more than three times that of CXO1415) can be partially explained by the difference in the temperatures of approximately 1.3 keV. Both clusters appear to be a factor of two less luminous than expected on the basis of the empirical, redshift-dependent  $L$ – $T$  relation of Vikhlinin et al. (2009). However, recent data of distant clusters support a weaker luminosity evolution with respect to that found in Vikhlinin et al.

**Table 2**  
Summary of the Mass Estimates for XDCP0044 Based on the  
Hydrostatic Equilibrium Equation (2)

$\Delta$	Radius (kpc)	$M_{\text{tot}}$ ( $M_{\odot}$ )	$M_{\text{ICM}}$ ( $M_{\odot}$ )
2500	$R_{2500} = 240^{+30}_{-20}$	$1.23^{+0.46}_{-0.27} \times 10^{14}$	$(8.2 \pm 1.1) \times 10^{12}$
...	$R_{\text{ext}} = 375$	$2.30^{+0.5}_{-0.3} \times 10^{14}$	$(1.48 \pm 0.2) \times 10^{13}$
500*	$R_{500} = 562^{+50}_{-37}$	$3.2^{+0.9}_{-0.6} \times 10^{14}$	$(2.5 \pm 0.3) \times 10^{13}$
200*	$R_{200} = 845^{+80}_{-50}$	$4.4^{+1.3}_{-0.8} \times 10^{14}$	$(3.8 \pm 0.5) \times 10^{13}$

**Notes.** The “\*” indicates that the mass values are extrapolated beyond the maximum radius  $R_{\text{ext}}$  where the ICM emission is actually measured. We assume a constant temperature profile within  $R_{\text{ext}}$  and a slowly decreasing profile as  $kT \propto r^{-0.24}$  at larger radii.

(2009) from a much smaller redshift range (see Reichert et al. 2011; Böhringer et al. 2012). A factor of two difference at this high redshift is consistent with this scenario and in line with preheating models.

The spectral analysis and the surface brightness analysis allow us to have a direct measure of the total ICM mass within the extraction radius  $R_{\text{ext}} = 375$  kpc, which yields  $M_{\text{ICM}} = (1.48 \pm 0.2) \times 10^{13} M_{\odot}$ . On the other hand, the total cluster mass can be estimated under the assumptions of hydrostatic equilibrium and spherical symmetry, which leads to the simple equation (Sarazin 1988):

$$M(r) = -4.0 \times 10^{13} M_{\odot} T(\text{keV}) r(\text{Mpc}) \times \left( \frac{d \log(n_e)}{d \log r} + \frac{d \log(T)}{d \log r} \right). \quad (2)$$

Since we are not able to measure the temperature profile, we assume isothermality inside the extraction radius, while beyond  $R_{\text{ext}}$  we adopt a mildly decreasing temperature profile  $kT \propto r^{-0.24}$ , as found in local clusters (see Leccardi & Molendi 2008). Therefore the term in parentheses in Equation (2) is the sum of the slope of the slowly declining temperature profile and the slope of the density profile, which is simply  $-3 \beta x^2/(1+x^2)$ , where  $x = r/r_c$ .

To measure the total mass at a given density contrast, we solve the equation  $M_{\Delta}(r_{\Delta}) = 4/3\pi r_{\Delta}^3 \Delta \rho_c(z_{cl})$ . This relation allows us to compute the radius where the average density level with respect to the critical density  $\rho_c(z_{cl})$  is  $\Delta$ . Virial mass measurements are typically reported for  $\Delta = 2500, 500$ , and 200. The  $1\sigma$  confidence intervals on the mass are computed by including the error on the temperature and on the gas density profile. The results are shown in Table 2. Only the radius  $r_{2500} = 240^{+30}_{-20}$  kpc is well within the detection region. We obtain  $M_{2500} = 1.23^{+0.46}_{-0.27} \times 10^{14} M_{\odot}$ . The total mass extrapolated to  $r_{500}$ , with the temperature profile gently decreasing beyond  $R_{\text{ext}} = 375$  kpc as  $\propto r^{-0.24}$ , is  $M_{500} = 3.2^{+0.9}_{-0.6} \times 10^{14} M_{\odot}$  for  $R_{500} = 562^{+50}_{-37}$  kpc. We also extrapolate the mass measurement up to the nominal virial radius, finding  $M_{200} = 4.4^{+1.3}_{-0.8} \times 10^{14} M_{\odot}$  for  $R_{200} = 845^{+80}_{-50}$  kpc. The ICM mass fraction within  $R_{\text{ext}}$  is  $f_{\text{ICM}} = 0.07 \pm 0.02$ , and  $f_{\text{ICM}} = 0.08 \pm 0.02$  at  $R_{500}$ . These values are in very good agreement with the empirical relation between  $f_{\text{ICM}}$  and  $M_{500}$  shown in Vikhlinin et al. (2009). In Table 2 we also report the mass measured at  $R_{\text{ext}} = 375$  kpc, which is the largest radius where we can obtain a robust measurement of the mass without extrapolations.

## 4. DISCUSSION

### 4.1. Systematics in Mass Measurements

The mass measurements at  $R_{500}$  and  $R_{200}$  have been obtained under the assumption of hydrostatic equilibrium as an extrapolation of the observed profile beyond the largest radius where X-ray emission is detected (375 kpc), as well as under some reasonable assumptions on the slope of the temperature profile declining as  $\propto r^{-0.24}$  outside the extraction radius, as observed in local clusters in the  $(0.1-0.6) \times r_{180}$  range (Leccardi & Molendi 2008). For completeness, we recompute the masses after relaxing the assumption of isothermality within the extraction radius and adopting the temperature profile  $kT \propto r^{-0.24}$  also for radii  $r < R_{\text{ext}}$ . In this case, the only requirement is that the average temperature within  $R_{\text{ext}}$  is 6.7 keV as observed. With these assumptions, masses at  $M_{500}$  and  $M_{200}$  are 25% and  $\sim 30\%$ , respectively, lower than those obtained with the simplest choice  $T = \text{const}$  for  $r < R_{\text{ext}}$ , while  $M_{2500}$  is lower only by 8%, being much more robust and anchored to the data. These differences should be regarded as systematic, since the temperature profile within the extraction radius may well behave differently from a simple power law, with significantly different effects on the extrapolated masses. In this work, given the uncertain temperature distribution in the ICM of XDCP0044 and the spatially resolved spectral analysis presented in Section 2.4, we conclude that the assumption of constant temperature within  $R_{\text{ext}}$  and the mass measurements presented in Table 2 should be considered as the most accurate. Clearly, the uncertainty associated with the temperature profile will be solved only when a robust, spatially resolved spectral analysis of distant X-ray clusters will be possible.

We also extrapolate the mass according to the Navarro, Frenk, and White profile (NFW; Navarro et al. 1996), after requiring a normalization at 375 kpc to the total mass value actually measured from the data. Still, the extrapolation depends on the unknown concentration parameter. However, such dependence is not strong and can be accounted for once we restrain the concentration to the plausible range  $c_{\text{NFW}} = 4.0 \pm 0.5$  (Gao et al. 2008) or  $c_{\text{NFW}} = 3.5 \pm 0.5$  (Duffy et al. 2008), as found in simulations for the wide mass range  $5 \times 10^{13} M_{\odot} < M < 5 \times 10^{14} M_{\odot}$  at high  $z$ . We find  $M_{500} = (3.7^{+1.5}_{-0.9}) \times 10^{14} M_{\odot}$  and  $M_{200} = (5.6^{+1.9}_{-1.7}) \times 10^{14} M_{\odot}$ . Here, the much larger error bars include both the propagation of the statistical error on the measured mass within  $R_{\text{ext}}$ , which is used to normalize the NFW profile, and the uncertainty on the concentration parameter.

### 4.2. Comparison with Empirical Calibrations

In order to evaluate the uncertainties on the estimate of  $M_{500}$  and  $M_{200}$  based on empirical relations, we present the mass estimates adopting four different calibrations. Clearly, here we are using the high- $z$  end of these calibrations, which have been obtained mostly on the basis of low- and medium- $z$  clusters. The first estimate is based on the redshift-dependent scaling relations calibrated on local clusters and presented in Vikhlinin et al. (2009). From the empirical relation described in their Table 3:

$$M_{500} = M_0 \times (kT/5 \text{ keV})^{\alpha} E(z)^{-1}, \quad (3)$$

where  $M_0 = (2.95 \pm 0.10) \times 10^{14} h^{-1} M_{\odot}$  and  $\alpha = 1.5$ . We find  $M_{500} = 2.8^{+0.8}_{-0.6} \times 10^{14} M_{\odot}$ , consistent well within  $1\sigma$  with our measurement based on the hydrostatic equilibrium equation. Another mass–temperature calibration, based on distant cluster

**Table 3**  
Total Mass Estimates of XDCP0044 at  $R_{500}$  and  $R_{200}$  Obtained through Empirical Calibrations

Method	$R_{500}$ (kpc)	$M_{500}$ ( $M_{\odot}$ )	$M_{200}$ ( $M_{\odot}$ )
$M$ – $T$ relation (1)	...	$2.8^{+0.8}_{-0.6} \times 10^{14}$	...
$M$ – $T$ relation (2)	...	...	$4.0^{+1.7}_{-1.4} \times 10^{14}$
$Y_X$ – $M$ relation (3)	$515 \pm 30$	$2.2^{+0.5}_{-0.4} \times 10^{14} M_{\odot}$	...
$Y_X$ – $M$ relation (4)	$580^{+45}_{-35}$	$3.3^{+0.4}_{-0.6} \times 10^{14} M_{\odot}$	...

**Note.** (1) Vikhlinin et al. (2009); (2) Reichert et al. (2011); (3) Vikhlinin et al. (2009); (4) Fabjan et al. (2011).

measurements (Reichert et al. 2011), provides an estimate for the virial mass  $M_{200} = 4.0^{+1.7}_{-1.4} \times 10^{14} M_{\odot}$ .

As a further method, we use the integrated pseudo-pressure parameter  $Y_X \equiv T_X \times M_{\text{ICM}}$ , which is considered a robust mass proxy within  $R_{500}$ , as shown by numerical simulations (e.g., Kravtsov et al. 2006). The observed value for XDCP004 is  $Y_X = (1.60 \pm 0.33) \times 10^{14} \text{ keV } M_{\odot}$ . We use the  $Y_X$ – $M$  empirical relation taken from Table 3 of Vikhlinin et al. (2009):

$$M_{500} = M_0 \times (Y_X / 3 \times 10^{14} M_{\odot} \text{ keV})^{\alpha} E(z)^{-2/5}, \quad (4)$$

where  $M_0 = (2.95 \pm 0.30) \times 10^{14} M_{\odot} h^{1/2}$  and  $\alpha = 0.6$ . We find  $M_{500} = (2.2^{+0.5}_{-0.4}) \times 10^{14} M_{\odot}$  and  $R_{500} = (515 \pm 30) \text{ kpc}$ . Using the calibration based on numerical simulations obtained in Fabjan et al. (2011), we find  $M_{500} = 3.3^{+0.4}_{-0.6} \times 10^{14} M_{\odot}$ , for  $R_{500} = 580^{+45}_{-35} \text{ kpc}$ . Both values are obtained iteratively in order to compute consistently all the quantities at  $r_{500}$ . Note, however, that  $Y_X$  should be measured between  $0.15 \times R_{500}$  and  $R_{500}$  and  $M_{\text{gas}}$  within  $R_{500}$ , while for XDCP0044 we measure the global temperature within  $R_{\text{ext}} < R_{500}$  and  $M_{\text{ICM}}$  is computed at  $R_{500}$  by extrapolating the best-fit  $\beta$  model. Therefore, our measured value of  $Y_X$  may differ from the true pseudo-pressure parameter. We also comment that the use of  $Y_X$  as a mass proxy at high redshift may require higher S/N.

The uncertainty among different calibrations can be appreciated in Table 3. We find that the uncertainty on  $M_{500}$  can amount to 20%, comparable to the  $1\sigma$  confidence level associated with the statistical uncertainty. We remark that mass estimates based on a  $\beta$ -profile fitting and the assumption of hydrostatic equilibrium may give values  $\sim 20\%$  lower around  $r_{500}$  (and even more discrepant for larger radii) due to the violation of hydrostatic equilibrium and the presence of significant bulk motions in the ICM. This has been shown in numerical simulations (see Bartelmann & Steinmetz 1996; Rasia et al. 2004; Borgani et al. 2004). Observational calibrations also show that hydrostatic masses underestimate weak-lensing masses by 10% on average at  $r_{500}$  (see Hoekstra 2007; Mahdavi et al. 2013). This is also found in numerical simulations (see Becker & Kravtsov 2011; Rasia et al. 2012). However, most recent works (von der Linden et al. 2014; Israel et al. 2014) find no hints of bias, at least in massive clusters, by comparing X-ray and weak-lensing masses.

Our conclusion is that the use of empirical calibrations to estimate  $M_{500}$  may suffer systematics of the order of 20%, comparable, in this case, to the statistical errors associated with the X-ray mass measurements. Estimates of  $M_{200}$  are more uncertain (30%–40%). A weak-lensing study will be crucial to assess the robustness of the X-ray mass estimate at  $R_{200}$  for this cluster. We expect this to be feasible with moderately

deep *Hubble Space Telescope* Advanced Camera for Surveys imaging, based on Jee et al. (2011).

#### 4.3. Cosmological Implications

Although several clusters have been confirmed at  $z \gtrsim 1.5$ , XDCP0044 is currently the only cluster at these redshifts whose diffuse X-ray emission provides constraints on the ICM temperature and on the mass. Because the expected number of hot clusters at such high redshift is extremely low, the mere presence of a few massive, high- $z$  galaxy clusters could create some tension with the standard  $\Lambda$ CDM and quintessence models (e.g., Jimenez & Verde 2009; Baldi & Pettorino 2011; Chongchitnan & Silk 2012; Mortonson et al. 2011; Harrison & Coles 2012; Waizmann et al. 2012). So far, no evidence for such a discrepancy has been found, except when considering the combined probability of the most massive, high- $z$  clusters (Jee et al. 2011). Therefore, it is important to investigate whether the presence of XDCP0044 is creating tension with the current  $\Lambda$ CDM paradigm of the large-scale structure formation.

It is straightforward to predict the abundance of massive clusters at  $z > z_{\text{min}}$  whose mass exceeds  $M > M_{\text{min}}$  by evaluating the following integral:

$$N(M, z) = f_{\text{sky}} \int_{z_{\text{min}}}^{z_{\text{max}}} \frac{dV(z)}{dz} dz \int_{M_{\text{min}}}^{M_{\text{max}}} \frac{dn}{dM} dM, \quad (5)$$

where  $dV/dz$  is the volume element per redshift interval,  $dn/dM$  is the mass function, and  $f_{\text{sky}}$  is the survey area normalized to give  $f_{\text{sky}} = 1$  for a full sky. In general,  $f_{\text{sky}}$  depends on the flux and therefore on the cluster mass and redshift, so that  $N(M, z)$  would depend on the convolution of  $f_{\text{sky}}$  with the mass function and the volume element. However, at present, we cannot model  $f_{\text{sky}}$  for the XDCP survey and we choose a constant, conservative value as explained below.

In this paper, we use the Tinker et al. (2008) mass function, which has been calibrated based on numerical simulations. We do not attempt to include the effects of baryon physics, which have been shown to be also relevant at cluster scales. In particular, it has been found that AGN feedback produces a lower mass function with respect to the DM-only case (Velliscig et al. 2014; Cui et al. 2014). Clearly, this effect would reduce the probability of finding massive clusters for a given set of cosmological parameters. Therefore, our choice of adopting the Tinker et al. (2008) mass function must be considered conservative. Finally, because the cluster X-ray emission is mostly confined within a few hundred kpc from the center, we evaluate the mass function using a contrast of  $\Delta = 600$  with respect to the critical density, which gives the cluster mass  $M_{600} \simeq 3.1 \times 10^{14} M_{\odot}$  at  $r_{600} = 530 \text{ kpc}$ .

The median flux limit of the XDCP survey is  $\sim 10^{-14} \text{ erg s}^{-1} \text{ cm}^{-2}$  in the 0.5–2 keV band, which we translate into a maximum detection redshift  $z_{\text{max}} \sim 2.2$ . We remind readers that the rarity of massive clusters at high redshift makes the evaluation of the integral not sensitive to the exact value of the redshift upper limit. For this flux limit, the best estimate of the effective survey area is  $\sim 70 \text{ deg}^2$  ( $f_{\text{sky}} \sim 1.7 \times 10^{-3}$ ). We stress that this choice corresponds to the assumption that the XDCP reaches a limiting flux of  $10^{-14} \text{ erg s}^{-1} \text{ cm}^{-2}$  over the entire solid angle. A more realistic treatment would give a lower  $f_{\text{sky}}$ , and correspondingly lower probabilities of finding such a massive cluster in the XDCP. Finally, the probability distribution is computed by setting our cluster’s redshift as the minimum value, therefore we are not considering the degeneracy between the  $M$  and  $z$  values for a given probability (see Hotchkiss 2011).



Adopting the above  $M_{600}$  as our threshold mass  $M_{\min}$ , we find that the probability of discovering at least one cluster with mass larger than  $M_{\min}$  and redshift higher than  $z_{\min}$  within the XDCP survey volume is  $\sim 3\%$  and  $\sim 6\%$  using the central values of the *WMAP* and Planck cosmological parameters, respectively. An interesting question is whether or not we should interpret this probability as indicating any tension with our  $\Lambda$ CDM paradigm. Obviously, in order to adequately propagate the discovery probability into cosmological tension, the following additional factors should be considered.

First, we need to take into account the statistical uncertainties of current cosmological parameter measurements. For example, if we increase the  $\sigma_8$  value by  $2\sigma$  ( $\sigma_8 = 0.882$ ), the probability becomes as high as  $\sim 16\%$ . Second, an Eddington bias may be a non-negligible factor for objects with a steep mass function. It is possible that our central value of  $kT = 6.7$  keV may be obtained by an up-scatter while the “true” temperature of the cluster is lower or that our result is given by a down-scatter from a higher temperature. Because of the steep mass function, the up-scatter is more likely than the down-scatter. Mortonson et al. (2011) suggested that one should use a lower (corrected) mass to properly compensate for the Eddington bias. Substituting the central value of our mass estimate into Equation 16 of Mortonson et al. (2011) reduces the above threshold mass by  $\sim 5\%$ . Therefore, in the current case the application of this correction does not critically affect our cluster abundance estimation. Third, one can question the validity of adopting the cluster redshift  $z = 1.58$  as  $z_{\min}$ . Using the cluster redshift is justified when we merely estimate the expected abundance of a similarly massive cluster beyond that redshift. However, for examining cosmological implications, one cannot exclude the volume at lower redshift, where more massive clusters with similar rarity can exist. Estimating a fair value for  $z_{\min}$  is challenging in general (e.g., priority in follow-up observations) and particularly so in the XDCP survey where observers preferentially look for faint, distant cluster emission in the archival data. Fourth, we should remember that current theoretical mass functions are obtained in  $N$ -body simulations, where extreme clusters are also rare. Consequently, the mass function is the result of extrapolation. Fifth, the current cluster mass is derived under hydrostatic equilibrium assumption. Although we have witnessed a case where the assumption may still hold for massive clusters such as XMMUJ2235 at  $z = 1.4$  (Rosati et al. 2009; Jee et al. 2009), the redshift  $z = 1.58$  is a regime where we expect a rapid evolution of ICM properties.

Considering the above factors, we conclude that it is premature to translate the rarity of XDCP0044 by itself into any tension with the current  $\Lambda$ CDM paradigm. However, it is still interesting to note that the relatively small XDCP survey have already discovered two extreme clusters: XDCP0044 and XMMUJ2235 at  $z = 1.58$  and  $1.4$ , respectively. The smaller ( $\sim 8$  deg<sup>2</sup>) IDCS survey found the cluster IDCS J1426.5+3508 at  $z = 1.75$ , whose discovery probability within that survey is  $\sim 1\%$  (Brodwin et al. 2012). The much larger (1000 deg<sup>2</sup>) ACT SZ survey discovered the “El Gordo” cluster  $z = 0.87$  (Menanteau et al. 2012) whose X-ray and weak-lensing masses indicate that the probability of discovering such a massive cluster is low ( $\sim 1\%$ ) even in the full sky (Jee et al. 2014). To summarize, there are hints that the detection of sparse, massive galaxy clusters at high redshift points toward inconsistencies of the standard  $\Lambda$ CDM model or a significantly higher normalization ( $\sigma_8$ ) parameter. However, more robust studies based on deep and complete samples of galaxy clusters are necessary to quantify the actual tension with

the  $\Lambda$ CDM. In this respect, SZ surveys, coupled to a robust mass calibration, may play a dominant role. Unfortunately, it is very hard to build deep and complete samples with current X-ray facilities, and the planned X-ray surveys in the near future will not be able to explore efficiently the high- $z$  range (see also Section 4.5).

#### 4.4. Substructure and Dynamical Status

A visual inspection of the residual ICM emission shows a clear elongation along the north–south axis. We already investigated in Sections 2.4 and 2.5 the possible existence of two clumps with different temperatures. We showed that both the spectral analysis and the azimuthally averaged surface brightness distribution suggest the presence of two distinct clumps constituting the bulk of the ICM. However, deeper data would be needed before reaching firm conclusions. In fact, it is impossible to decide whether the elongation and the two-region structure are due to an ongoing merger between comparable mass halos or simply to a young dynamical status. If the typical formation epoch of massive clusters is  $z \lesssim 2$ , the age of XDCP0044 is less than 0.8 Gyr, a timescale which is shorter than its dynamical time. In this scenario, we expect to observe significant differences in virialized, massive clusters in the  $1.5 < z < 2.0$  range, since the time elapsed from the first virialization process is smaller than their dynamical timescales.

To further investigate the presence of substructures in the ICM distribution, we remove the best fit  $\beta$ -model from the X-ray image to obtain the residual image. In Figure 10 we show the smoothed X-ray image of XDCP0044 in the soft band, a simulated image of the best fit model and the residual image, obtained subtracting an average of  $10^4$  simulated images from the real data. The FOV of the three images is a square with a side of  $\sim 90''$ , corresponding to 180 pixels (1 pixel corresponds to  $0''.492$ ). In the smoothed image, the surface brightness distribution appears to be clumpy along the direction of the elongation, and this appears more clearly in the residual image. However, the statistical significance of the clumps must be carefully evaluated before drawing any conclusion.

To assess the significance of the fluctuations in the X-ray surface brightness of XDCP0044, we proceed as follows. First we create  $\sim 10,000$  X-ray images obtained directly as random realizations from the best fit  $\beta$ -model. We use the same background and the same number of total counts from the real soft-band image, in order to reproduce the same level of noise in the data. We also convolve the simulated images with the normalized, soft-band exposure map, in order to take into account any possible feature due to variations of the effective area. This set of images can be compared with the XDCP0044 soft-band image, where all the unresolved sources previously identified have been removed and the corresponding extraction regions are filled with photons, consistently with the surrounding surface brightness level. We verify a posteriori that this procedure does not introduce artificial features in the XDCP0044 image. As a simple but effective estimate of the amount of substructures in the simulated images, we compute the power spectrum as a function of  $|K|$ , the magnitude of the wavenumber vector. This is accomplished by computing the Fast Fourier Transform of each image and averaging power over circles of diameter  $|K|$ . We choose an image size of  $320 \times 320$  pixels, corresponding to  $157''.4$ . The expected spectrum from the best-fit  $\beta$ -model is computed averaging over the  $10^4$  simulated images. The crucial information is not only the average power spectrum, but also its

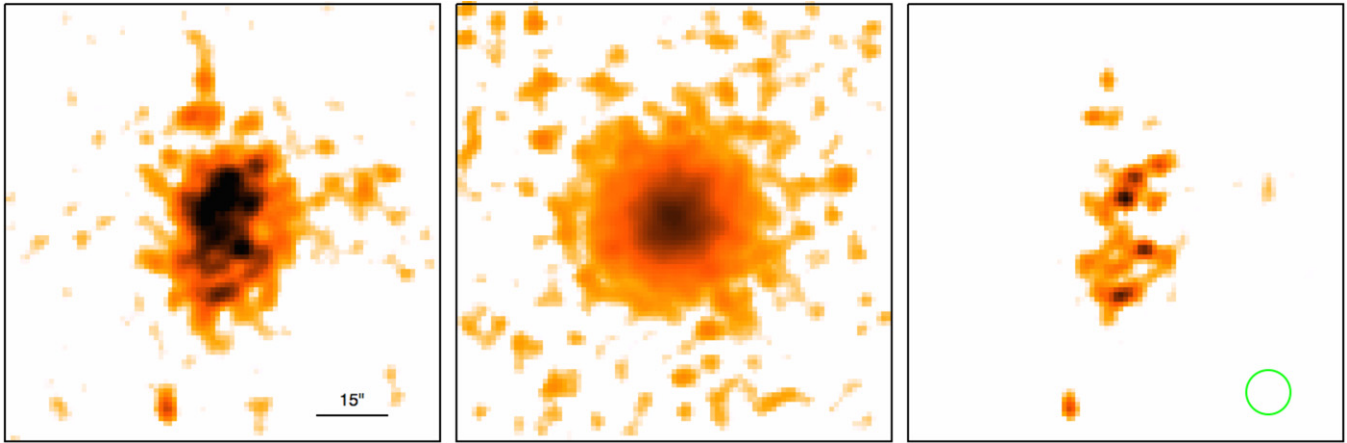


**Figure 10.** Left panel: smoothed X-ray image of XDCP0044 in the soft (0.5–2 keV) band after removing the identified unresolved sources. Central panel: simulated soft-band image from the best-fit  $\beta$  model. Right panel: map of the X-ray residual in the soft band obtained subtracting the simulated  $\beta$ -model image from the X-ray image. All images are  $90''$  across. The circle in the lower right of the third panel corresponds to a radius of  $\sim 40$  kpc, which is the scale where we found evidence of substructures in the ICM.

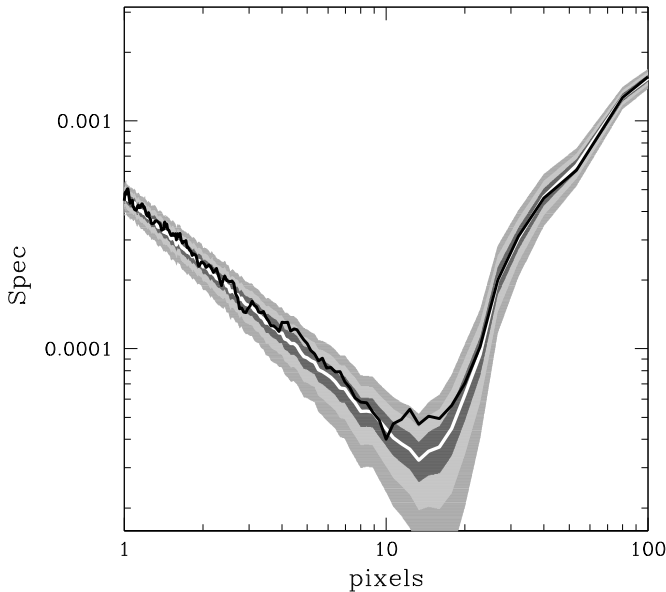


**Figure 11.** Radially averaged power spectrum of the soft-band image of XDCP0044 (black solid line) is compared to the expected power spectrum of the image of the best-fit  $\beta$ -model, obtained as an average over  $10^4$  simulated images. The power spectrum is shown as a function of the physical scale (in pixels). The size of the each simulated image is  $320 \times 320$  pixels, corresponding to  $157'' \times 157''$ . The shaded areas corresponds to  $1\sigma$ ,  $2\sigma$  and  $3\sigma$  confidence (from dark to light gray). We notice a  $\sim 2\sigma$  excess in the data with respect to the model for scales between 10 and 20 pixels.

variance due to the actual S/N of the images. In Figure 11 we show the average power spectrum of the simulated images and its variance. We also compute the two-dimensional (2D) average power spectrum of the real image of XDCP0044, which is also shown in Figure 11 as a black continuous line. We notice a  $\sim 2\sigma$  excess in the data with respect to the model corresponding to scales between 10 and 20 pixels.

In order to better understand this result, we use another set of simulations, obtained by adding holes and bumps to the best-fit  $\beta$ -model. The holes and bumps are modeled as circular, randomly placed top-hat cavities or enhancements in the surface brightness distribution. These substructures are concentrated toward the cluster center, and only a limited number of configurations are simulated, which limit our investigation of

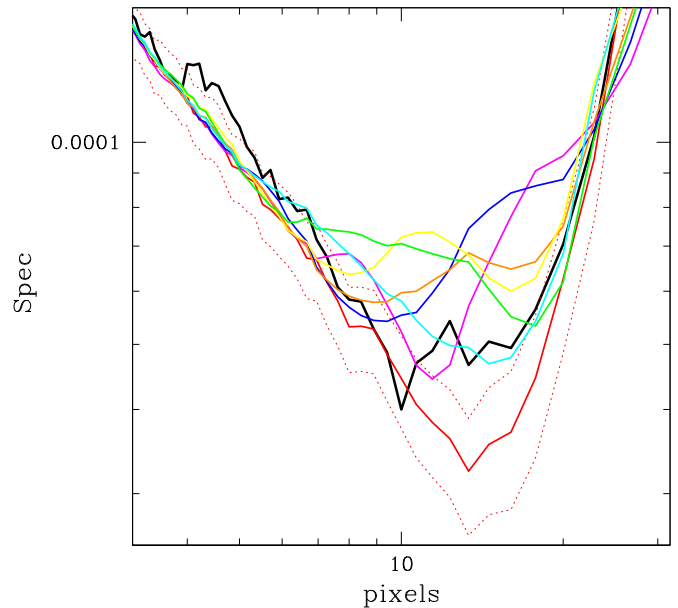


**Figure 12.** Radially averaged power spectrum of the soft-band image of XDCP0044 (black solid line) is compared to the expected power spectrum of the image of the best-fit  $\beta$ -model with top-hat perturbations with a radius of 5, 7, 8, 9, 10, and 15 pixels, shown as cyan, yellow, green, orange, blue, and magenta lines, respectively. The average power spectrum of the best-fit images and its  $1\sigma$  uncertainty are shown with red solid and dashed lines, respectively.

possible substructures in the surface brightness of the ICM. However, our procedure is adequate for a first characterization of the typical scale of the substructures. The results are shown in Figure 12, where we show the color-coded average power spectra of the simulated images with top-hat perturbations with a radius of 5, 7, 8, 9, 10, and 15 pixels. For clarity, the amplitude of the artificial perturbations in the simulations is larger than that expected in real data. As already mentioned, the size, position, and number of top-hat perturbations give rise to different spectral shape. Therefore, it is not straightforward to identify the typical perturbation scale directly from a visual inspection of the 2D averaged power spectrum. However, a clear trend is observed from the smallest to the largest scales. A comparison with the spectrum of the real data suggests that the  $\sim 2\sigma$  excess present in the power spectrum of the XDCP0044 image can be

ascribed to roughly circular fluctuations with radius of  $\sim 9$  pixels, corresponding to a physical scale of about 40 kpc. In the third panel of Figure 10 we show a circle with a 40 kpc radius for a direct comparison with the residual image.

In summary, we find  $2\sigma$  evidence of substructures in the surface brightness distribution of XDCP0044, compatible with circular, top-hat perturbations with a typical radius of 40 kpc. This can be interpreted as the presence of ICM clumps associated with relatively recent merging, but also with the presence of cavities. We stress that, despite the relatively low S/N of high- $z$  clusters observations, a statistical analysis of their surface brightness fluctuations is still possible with *Chandra*. The extension of this analysis to the overall high- $z$  cluster population will be presented elsewhere.

#### 4.5. Future Surveys and High- $z$ Clusters

Clusters of galaxies at high redshift ( $z > 1$ ) are vitally important to understand the evolution of the large scale structure of the universe, the processes shaping galaxy populations, and the cycle of the cosmic baryons, and to constrain cosmological parameters. At present, we know that at  $z > 1$  many massive clusters are fully virialized and their ICM is already enriched with metals. The present study extends this picture to  $z \sim 1.6$ . In the near future, it is possible that new studies will reveal virialized clusters at larger redshift and more massive than XDCP0044 (for example IDCS1426 at  $z = 1.75$ , which has been awarded a deep *Chandra* exposure in GO 14; Stanford et al. 2012).

Clearly, the small number statistics prevents us to draw quantitative conclusions on the evolutionary behavior in the range  $1 < z < 1.6$ , namely the evolution of the iron abundance and the evolution of the cool core phenomenon. The assembly of a large and well-characterized sample of high- $z$  X-ray clusters is a major goal for the future. For a basic characterization of an X-ray cluster, we consider the collection of about 1500 net photons in the 0.5–7 keV band with high angular resolution (point spread function HEW  $\sim 1''$ – $2''$ ) images to remove the effect of contaminating AGN emission and identify central cool cores. These requirements can provide a robust measurement of  $M_{2500}$  and a reliable estimate of  $M_{500}$ , necessary to perform cosmological tests.

The present study provides the first characterization of a massive cluster at a redshift as high as 1.6, but, at the same time, clearly shows that the realm of high- $z$  clusters ( $z \sim 1.5$  and higher, when the lookback time is larger than 9 Gyr) requires very time-expensive observations even with a major X-ray facility like *Chandra*. At present only *Chandra* has the angular resolution needed to achieve an in-depth analysis of the ICM properties of distant clusters. In the near future it is likely that the number of detections of high- $z$  X-ray clusters will increase to several tens on the basis of the still growing *Chandra* and *XMM-Newton* archives. However, the number of high- $z$  X-ray clusters with a robust physical characterization and measured hydrostatic masses will be much lower given its very high cost in terms of observing time.

The perspective for distant cluster studies is not expected to improve much on the basis of currently planned missions. Looking at the near future, the upcoming mission eROSITA (Predehl et al. 2010; Merloni et al. 2012) will finally provide an X-ray all-sky coverage 20 years after the *ROSAT* All Sky Survey (Voges et al. 1999), down to limiting fluxes more than one order of magnitude lower than *ROSAT* for extended sources, therefore considerably increasing the number of low- and moderate-redshift clusters. However, the limiting flux after four years

of operation is predicted to be  $3.4 \times 10^{-14}$  erg s $^{-1}$  cm $^{-2}$ , well above the  $10^{-14}$  erg s $^{-1}$  cm $^{-2}$  flux level below which the majority of the distant cluster population lie. A sensitivity level of  $10^{-14}$  erg s $^{-1}$  cm $^{-2}$  will be reached only in the pole regions on  $\sim 140$  deg $^2$ , a solid angle which is already covered by the extragalactic *Chandra* archive at better fluxes and much better angular resolution. Therefore, in the near future the number of new high-redshift clusters will be mainly provided by SZ observations and other near-IR large-area surveys, some of which are already delivering an increasing number of clusters at  $z > 1$  (see Rettura et al. 2014). However, X-ray observations will still be required for a physical characterization of these systems, mass calibration, and a wide range of astrophysical and cosmological applications.

Only a wide-field, high angular resolution X-ray mission with a large collecting area and good spectral resolution up to 7 keV seems to be able to match such requirements (see the WFXT; Murray et al. 2010). The combination of good angular resolution and a constant image quality across a 1 deg $^2$  FOV, coupled with a large effective area and a survey-oriented strategy, can provide a direct measurement of temperatures, density profiles, and redshifts for at least 1000 if not several thousand X-ray clusters at  $z > 1$ , depending on the survey strategy. We stress that the capability to perform detailed studies for  $z > 1$  clusters critically depends on the angular resolution, to avoid the confusion limit down to fluxes much lower than  $10^{-14}$  erg s $^{-1}$  cm $^{-2}$ . In addition, the capability of measuring the X-ray redshift directly from the X-ray analysis of the ICM emission would avoid a time-prohibitive optical spectroscopic follow-up program. This kind of mission would improve by almost two orders of magnitude any well-characterized cluster sample that we can possibly assemble using the entire wealth of data from present and planned X-ray facilities.

In the distant future (15–20 yr) major X-ray missions like Athena (Barcons et al. 2012; Nandra et al. 2013) and SMART-X can provide surveys with the required depth and quality, by devoting a significant amount of their lifetime to such a program. In particular, if used in survey mode, the current design of SMART-X with a large FOV CMOS detector would be comparable with WFXT. Clearly, the characteristics of SMART-X are best suited for a follow-up campaign of, let us say, SZ-selected clusters, rather than for an X-ray survey. In general, given their optics and their instrument setup, it is not very efficient to use these two major X-ray facilities in survey mode. Also, Athena or SMART-X surveys will be available much later than the many wide surveys that will dominate Galactic and extragalactic astronomy in the next decade (Pan-STARRS, LSST, Euclid, JVLA, SKA). To summarize, even though eROSITA will provide a crucial and vital all-sky survey in the soft X-ray band, all scientific cases concerning objects in the faint flux regime (about  $10^{-14}$  erg cm $^{-2}$  s $^{-1}$  and below), or requiring substantial information above 2 keV, has to rely on archival data of *Chandra* and *XMM-Newton*.

## 5. CONCLUSIONS

We presented a deep X-ray observation of the most massive distant X-ray cluster of galaxies currently known. XDCP0044 was discovered in the XDCP survey and imaged in a 380 ks *Chandra* ACIS-S exposure aimed at measuring its mass and studying its ICM properties. We are able to obtain a robust measure of the ICM temperature and total mass within 375 kpc and a reliable extrapolation up to  $R_{500}$ . We are also able to



investigate the presence of substructures in the ICM distribution. Here we summarize our main results:

1. XDCP0044 is detected with  $S/N \sim 20$  within a circle with a radius of  $44''$ , corresponding to 375 kpc at  $z = 1.58$ . The azimuthally averaged surface brightness distribution can be well described by a  $\beta$  model with  $\beta = 0.75$  and  $r_c = 99$  kpc; the soft-band flux within  $r = 44''$  is equal to  $S_{0.5-2.0\text{keV}} = (1.66 \pm 0.01) \times 10^{-14} \text{ erg s}^{-1} \text{ cm}^{-2}$ ;
2. the spectral fit with a `mekal` model gives a global temperature  $kT = 6.7^{+1.3}_{-0.9} \text{ keV}$  and a global iron abundance  $Z_{\text{Fe}} = 0.41^{+0.29}_{-0.26} Z_{\odot}$ ;
3. despite the iron emission line being measured with a confidence level lower than  $2\sigma$ , the upper limits found for the iron abundance are in agreement with a mild, negative evolution of about a factor 1.5–2 between  $z = 0$  and  $z \sim 1$  as found in previous *Chandra* and *XMM-Newton* studies (Balestra et al. 2007; Maughan et al. 2008; Anderson et al. 2009; Baldi et al. 2012), and, at the same time, with a non-negligible chemical enrichment at a level of  $\sim 0.2\text{--}0.4 Z_{\text{Fe}\odot}$ , comparable to local clusters;
4. the total mass measured at  $R_{2500} = (240^{+30}_{-20}) \text{ kpc}$  is  $M_{2500} = 1.23^{+0.46}_{-0.27} \times 10^{14} M_{\odot}$ . The total mass is reliably measured out to 375 kpc, where it amounts to  $M(r < 375 \text{ kpc}) = 2.30^{+0.50}_{-0.30} \times 10^{14} M_{\odot}$ , while the ICM mass is  $M_{\text{ICM}}(r < 375 \text{ kpc}) = (1.48 \pm 0.2) \times 10^{13} M_{\odot}$ , resulting in an ICM mass fraction  $f_{\text{ICM}} = 0.07 \pm 0.02$ ;
5. assuming a mildly decreasing temperature profile at  $r > R_{\text{ext}}$  as observed in local clusters, we are able extrapolate the mass measurement up to  $R_{500} = 562^{+50}_{-37} \text{ kpc}$ , finding  $M_{500} = 3.2^{+0.9}_{-0.6} \times 10^{14} M_{\odot}$ ; this value is consistent with those obtained using empirical relations between X-ray observables and total mass;
6. a detailed analysis of the surface brightness distribution reveals the presence of two clumps, with marginally different temperatures, which may be due to a recent merger or to a young dynamical status; we do not find evidence for the presence of a cool core; the average values of the entropy  $\sim 94^{+19}_{-14} \text{ keV cm}^{-2}$  and of the cooling time  $4.0^{+0.9}_{-0.6} \text{ Gyr}$  within 100 kpc confirm the lack of a cool core;
7. we also find some evidence ( $2\sigma$  c.l.) for clumping in the surface brightness distribution on scales  $\sim 40 \text{ kpc}$ , which may be interpreted as the signature of a not fully relaxed dynamical status, possibly due to the young age of the cluster;
8. when compared with the expectations for a  $\Lambda\text{CDM}$  universe based on the mass function of Tinker et al. (2008), XDCP0044 appears to be a typical cluster at  $z \sim 1.6$  for a *WMAP* cosmology (Komatsu et al. 2011); however, the redshift and the total mass of XDCP0044 make it the most massive galaxy cluster identified at  $z > 1.5$ .

The comparison of the ICM properties and of the galaxy population in this cluster, which will be presented in a series of future papers, may cast new light on the formation epoch of massive clusters, when processes like chemical enrichment, feedback from AGN, induced starbursts in the member galaxies, and merger events combine together in a short but hectic epoch. A systematic study of the distant cluster population, which is currently beyond the capability of the present-day X-ray facilities without a prohibitive investment of observing time, will reveal a huge wealth of complex processes whose comprehension is mandatory for a complete picture of cosmic structure formation.

We acknowledge financial contribution from contract PRIN INAF 2012 (“A unique data set to address the most compelling open questions about X-ray galaxy clusters”), and PRIN MIUR 2009 (“*Tracing the growth of structures in the Universe*”). H.B. acknowledges support from the DFG Transregio program “Dark Universe” and the Munich Excellence Cluster “Structure and Evolution of the Universe”. This work was carried out with *Chandra* Program 14800360 obtained in AO14. J.S.S. acknowledges funding from the European Union Seventh Framework Programme (FP7/2007-2013) under grant agreement number 267251 Astronomy Fellowships in Italy (AstroFit). We acknowledge the hospitality of Villa Il Gioiello (Arcetri, Florence), which is part of the agreement regarding the Colle di Galileo, where some of the results presented here were discussed. Finally, we thank the referee, Pasquale Mazzotta, for his careful and critical reading of this manuscript.

## REFERENCES

- Anderson, M. E., Bregman, J. N., Butler, S. C., & Mullis, C. R. 2009, *ApJ*, **698**, 317
- Andersson, K., Benson, B. A., Ade, P. A. R., et al. 2011, *ApJ*, **738**, 48
- Andreon, S., Maughan, B., Trinchieri, G., & Kurk, J. 2009, *A&A*, **507**, 147
- Arnaud, K. A. 1996, in ASP Conf. Ser. 101, *Astronomical Data Analysis Software and Systems V*, ed. G. H. Jacoby & J. Barnes (San Francisco, CA: ASP), 17
- Asplund, M., Grevesse, N., & Sauval, A. J. 2005, in ASP Conf. Ser. 336, *Cosmic Abundances as Records of Stellar Evolution and Nucleosynthesis* ed. T. G. Barnes, III & F. N. Bash (San Francisco, CA: ASP), 25
- Baldi, A., Ettori, S., Molendi, S., et al. 2012, *A&A*, **537**, A142
- Baldi, M., & Pettorino, V. 2011, *MNRAS*, **412**, L1
- Balestra, I., Tozzi, P., Ettori, S., et al. 2007, *A&A*, **462**, 429
- Barcons, X., Barret, D., Decourchelle, A., et al. 2012, *arXiv:1207.2745*
- Barkhouse, W. A., Green, P. J., Vikhlinin, A., et al. 2006, *ApJ*, **645**, 955
- Bartelmann, M., & Steinmetz, M. 1996, *MNRAS*, **283**, 431
- Bayliss, M. B., Ashby, M. L. N., Ruel, J., et al. 2014, *ApJ*, **794**, 12
- Becker, M. R., & Kravtsov, A. V. 2011, *ApJ*, **740**, 25
- Bignamini, A., Tozzi, P., Borgani, S., Ettori, S., & Rosati, P. 2008, *A&A*, **489**, 967
- Böhringer, H., Dolag, K., & Chon, G. 2012, *A&A*, **539**, A120
- Borgani, S., Murante, G., Springel, V., et al. 2004, *MNRAS*, **348**, 1078
- Brodwin, M., Gonzalez, A. H., Stanfor, S. A., et al. 2012, *ApJ*, **753**, 162
- Brodwin, M., Stern, D., Vikhlinin, A., et al. 2011, *ApJ*, **732**, 33
- Cavaliere, A., & Fusco-Femiano, R. 1976, *A&A*, **49**, 137
- Chongchitnan, S., & Silk, J. 2012, *PhRvD*, **85**, 063508
- Clerc, N., Sadibekova, T., Pierre, M., et al. 2012, *MNRAS*, **423**, 3561
- Condon, J. J., Cotton, W. D., Greisen, E. W., et al. 1998, *AJ*, **115**, 1693
- Cui, W., Borgani, S., & Murante, G. 2014, *MNRAS*, **441**, 1769
- De Grandi, S., Santos, J. S., Nonino, M., et al. 2014, *A&A*, **567**, 102
- Demarco, R., Wilson, G., Muzzin, A., et al. 2010, *ApJ*, **711**, 1185
- Donahue, M., Voit, G. M., Mahdavi, A., et al. 2014, *ApJ*, **794**, 136
- Duffy, A. R., Schaye, J., Kay, S. T., & Dalla Vecchia, C. 2008, *MNRAS*, **390**, L64
- Ettori, S., & Balestra, I. 2009, *A&A*, **496**, 343
- Fabjan, D., Borgani, S., Rasia, E., et al. 2011, *MNRAS*, **416**, 801
- Fassbender, R., Böhringer, H., Nastasi, A., et al. 2011a, *NJPh*, **13**, 125014
- Fassbender, R., Nastasi, A., Böhringer, H., et al. 2011b, *A&A*, **527**, L10
- Fassbender, R., Nastasi, A., Santos, J. S., et al. 2014, *A&A*, **568**, A5
- Finoguenov, A., Guzzo, L., Hasinger, G., et al. 2007, *ApJS*, **172**, 182
- Foley, R. J., Andersson, K., Bazin, G., et al. 2011, *ApJ*, **731**, 86
- Gao, L., Navarro, J. F., Cole, S., et al. 2008, *MNRAS*, **387**, 536
- Gobat, R., Daddi, E., Onodera, M., et al. 2011, *A&A*, **526**, A133
- Harrison, I., & Coles, P. 2012, *MNRAS*, **421**, L19
- Hoekstra, H. 2007, *MNRAS*, **379**, 317
- Hotchkiss, S. 2011, *JCAP*, **07**, 004
- Israel, H., Reiprich, T. H., Erben, T., et al. 2014, *A&A*, **564**, 129
- Jee, M. J., Dawson, K. S., Hoekstra, H., et al. 2011, *ApJ*, **737**, 59
- Jee, M. J., Hughes, J. P., Menanteau, F., et al. 2014, *ApJ*, **785**, 20
- Jee, M. J., Rosati, P., Ford, H. C., et al. 2009, *ApJ*, **704**, 672
- Jimenez, R., & Verde, L. 2009, *PhRvD*, **80**, 127302
- Kaastra, J. 1992, An X-Ray Spectral Code for Optically Thin Plasmas (Internal SRONLeiden Report, updated version 2.0)
- Kalberla, P. M. W., Burton, W. B., Hartmann, D., et al. 2005, *A&A*, **440**, 775

- Komatsu, E., Smith, K. M., Dunkley, J., et al. 2011, *ApJS*, **192**, 18
- Kravtsov, A. V., Vikhlinin, A., & Nagai, D. 2006, *ApJ*, **650**, 128
- Leccardi, A., & Molendi, S. 2008, *A&A*, **487**, 461
- Liedahl, D. A., Osterheld, A. L., & Goldstein, W. H. 1995, *ApJL*, **438**, L115
- Mahdavi, A., Hoekstra, H., Babul, A., et al. 2013, *ApJ*, **767**, 116
- Maughan, B. J., Jones, C., Forman, W., & Van Speybroeck, L. 2008, *ApJS*, **174**, 117
- Menanteau, F., Hughes, J. P., Sifón, C., et al. 2012, *ApJ*, **748**, 7
- Merloni, A., Predehl, P., Becker, W., et al. 2012, arXiv:1209.3114
- Mortonson, M. J., Hu, W., & Huterer, D. 2011, *PhRvD*, **83**, 023015
- Mullis, C. R., Rosati, P., Lamer, G., et al. 2005, *ApJL*, **623**, L85
- Murray, S. S., Giacconi, R., Ptak, A., et al. 2010, *Proc. SPIE*, **7732**, 77321W
- Nandra, K., Barret, D., Barcons, X., et al. 2013, arXiv:1306.2307
- Nastasi, A., Böhringer, H., Fassbender, R., et al. 2014, *A&A*, **564**, A17
- Nastasi, A., Fassbender, R., Böhringer, H., et al. 2011, *A&A*, **532**, L6
- Navarro, J. F., Frenk, C. S., & White, S. D. M. 1996, *ApJ*, **462**, 563
- Nousek, J. A., & Shue, D. R. 1989, *ApJ*, **342**, 1207
- Papovich, C., Momcheva, I., Willmer, C. N. A., et al. 2010, *ApJ*, **716**, 1503
- Pierini, D., Šuhada, R., Fassbender, R., et al. 2012, *A&A*, **540**, A45
- Pierre, M., Chiappetti, L., Pacaud, F., et al. 2007, *MNRAS*, **382**, 279
- Pierre, M., Clerc, N., Maughan, B., et al. 2012, *A&A*, **540**, A4
- Planck Collaboration, Ade, P. A. R., Aghanim, N., et al. 2011, *A&A*, **536**, A11
- Planck Collaboration, Ade, P. A. R., Aghanim, N., et al. 2013, *A&A*, **550**, A129
- Predehl, P., Böhringer, H., Brunner, H., et al. 2010, in AIP Conf. Proc. 1248, X-ray Astronomy 2009; Present Status, Multi-wavelength Approach and Future Perspectives, ed. A. Comastri, L. Angelini, & M. Cappi (Melville, NY: AIP), 543
- Rasia, E., Meneghetti, M., Martino, R., et al. 2012, *NJPh*, **14**, 055018
- Rasia, E., Tormen, G., & Moscardini, L. 2004, *MNRAS*, **351**, 237
- Reichert, A., Böhringer, H., Fassbender, R., & Mühlegger, M. 2011, *A&A*, **535**, A4
- Rettura, A., Martinez-Manso, J., Stern, D., et al. 2014, arXiv:1404.0023
- Rosati, P., Borgani, S., & Norman, C. 2002, *ARA&A*, **40**, 539
- Rosati, P., Tozzi, P., Ettori, S., et al. 2004, *AJ*, **127**, 230
- Rosati, P., Tozzi, P., Gobat, R., et al. 2009, *A&A*, **508**, 583
- Santos, J. S., Altieri, B., Valtchanov, I., et al. 2015, *MNRAS*, **447**, L65
- Santos, J. S., Fassbender, R., Nastasi, A., et al. 2011, *A&A*, **531**, L15
- Santos, J. S., Rosati, P., Gobat, R., et al. 2009, *A&A*, **501**, 49
- Santos, J. S., Rosati, P., Tozzi, P., et al. 2008, *A&A*, **483**, 35
- Santos, J. S., Tozzi, P., Rosati, P., Nonino, M., & Giovannini, G. 2012, *A&A*, **539**, A105
- Sarazin, C. L. 1988, X-ray Emission from Clusters of Galaxies (Cambridge: Cambridge Univ. Press)
- Sartoris, B., Borgani, S., Fedeli, C., et al. 2010, *MNRAS*, **407**, 2339
- Sifón, C., Menanteau, F., Hasselfield, M., et al. 2013, *ApJ*, **772**, 25
- Stalder, B., Ruel, J., Suhada, R., et al. 2013, *ApJ*, **763**, 93
- Stanford, S. A., Brodwin, M., Gonzalez, A. H., et al. 2012, *ApJ*, **753**, 164
- Stanford, S. A., Holden, B., Rosati, P., et al. 2001, *ApJ*, **552**, 504
- Stanford, S. A., Holden, B., Rosati, P., et al. 2002, *AJ*, **123**, 619
- Stanford, S. A., Romer, A. K., Sabirli, K., et al. 2006, *ApJL*, **646**, L13
- Tinker, J., Kravtsov, A. V., Klypin, A., et al. 2008, *ApJ*, **688**, 709
- Tozzi, P. 2013, *MmSAI*, **84**, 747
- Tozzi, P., Moretti, A., Tundo, E., et al. 2014, *A&A*, **567**, A89
- Tozzi, P., Santos, J. S., Nonino, M., et al. 2013, *A&A*, **551**, A45
- Tundo, E., Moretti, A., Tozzi, P., et al. 2012, *A&A*, **547**, A57
- Velliscig, M., van Daalen, M. P., Schaye, J., et al. 2014, *MNRAS*, **442**, 2641
- Vikhlinin, A., Kravtsov, A. V., Burenin, R. A., et al. 2009, *ApJ*, **692**, 1060
- Voges, W., Aschenbach, B., Boller, T., et al. 1999, *A&A*, **349**, 389
- von der Linden, A., Allen, M. T., Applegate, D. E., et al. 2014, *MNRAS*, **439**, 2
- Waizmann, J.-C., Ettori, S., & Moscardini, L. 2012, *MNRAS*, **422**, 3554
- Yu, H., Tozzi, P., Borgani, S., Rosati, P., & Zhu, Z.-H. 2011, *A&A*, **529**, A65
- Zeimann, G. R., Stanford, S. A., Brodwin, M., et al. 2012, *ApJ*, **756**, 115